sustainability

MDPI

Article

Spatiotemporal Interpolation of Actual Evapotranspiration Across Turkey Using the Australian National University Spline Model: Insights into Its Relationship with Vegetation Cover

İsmet Yener

Department of Forest Engineering, Faculty of Forestry, Artvin Coruh University, Artvin 08100, Turkey; yener@artvin.edu.tr

Abstract: Accurate and precise prediction of actual evapotranspiration (AET) on a large scale is a fundamental issue in natural sciences such as forestry (especially in species selection and planning), hydrology, and agriculture. With the estimation of AET, controlling dams, agriculture, and irrigation and providing potable and utility water supply for industry would be possible. Gathering reliable AET data is possible only with a sufficient weather station network, which is rarely established in many countries like Turkey. Therefore, climate models must be developed for reliable AET data, especially in countries with complex terrains. This study aimed to generate spatiotemporal AET surfaces using the Australian National University spline (ANUSPLIN) model and compare the results with the maps generated by the inverse distance weighting (IDW) and co-kriging (KRG) interpolation techniques. Findings from the interpolated surfaces were validated in three ways: (1) some diagnostics from the surface fitting model include measures such as signal, mean, root mean square predictive error, root mean square error estimate, root mean square residual of the spline, and the estimated standard deviation of noise in the spline; (2) a comparison of common error statistics between the interpolated surfaces and withheld climate data; and (3) evaluation by comparing model results with other interpolation methods using metrics such as mean absolute error, mean error, root mean square error, and adjusted R^2 (R^2_{adj}). The correlation between AET and normalized difference vegetation index (NDVI) was also evaluated. ANUSPLIN outperformed the other techniques, accounting for 73 to 94% (RMSE: 3.7 to 26.1%) of the seasonal variation in AET with an annual value of 83% (RMSE: 10.0%). The correlation coefficient between observed and predicted AET based on NDVI ranged from 0.49 to 0.71 for point-based and 0.62 to 0.83 for polygon-based data. The generated maps at a spatial resolution of $0.005° \times 0.005°$ could provide valuable insights to researchers and practitioners in the natural resources management domain.

Keywords: ANUSPLIN; IDW; kriging; NDVI; biome; climate change; evapotranspiration

check for updates

Academic Editor: Hossein Bonakdari

Received: 25 November 2024
Revised: 20 December 2024
Accepted: 27 December 2024
Published: 8 January 2025

Citation: Yener, İ. Spatiotemporal Interpolation of Actual Evapotranspiration Across Turkey Using the Australian National University Spline Model: Insights into Its Relationship with Vegetation Cover. *Sustainability* **2025**, *17*, 430. https://doi.org/10.3390/su17020430

1. Introduction

Evapotranspiration (ET) is the essential process that controls the water cycle and energy transmission between the hydrosphere, atmosphere, and biosphere [1]. ET comprises land surface evaporation and vegetation transpiration, which are critical in land-atmosphere interactions [2]. While evaporation refers to the moisture loss from water and soil surfaces to the atmosphere, transpiration refers to the loss from plant surfaces through stomata. Researchers examine ET as actual (AET) and potential evapotranspiration (PET). The former refers to the existing water loss realized under given or specific surfaces and atmospheric conditions. The latter implies water loss from ideal soil moisture, vegetation, and atmospheric conditions. PET provides initial insights on agricultural production and precautions for irrigation location, whereas AET delivers crucial information to determine soil moisture conditions and regional water balance [3]. Since AET is also responsible for the precipitation occurring at the base of the mountain range [4], water management requires quantifying water resources and understanding the water cycle, especially in semiarid and arid regions, where the low and irregular precipitation is largely returned to the atmosphere by AET [5]. After subtracting the AET loss, a region must know whether the remaining rainfall is sufficient, especially for plant growth and potable water [6]. AET, under the combined effect of climatic energy, capillary soil, and moisture availability, is also one of the most critical climate parameters controlling organic matter decomposition, returning to plant nutrients in terrestrial ecosystems and plant growth [7]. For example, AET accounted for 51% of the variation in the Scots pine forests' litter decomposition [8]. Therefore, it is crucial that AET be accurately determined [9]. The AET process is spatially and temporally dynamic. The quantification requirement of water resources is increasingly essential as anthropogenic impacts on land use and climate increase. However, it is challenging due to the water cycle's complex spatial and temporal variability [5].

Periodic and accurate determination or estimation of AET at the regional scale is crucial to promote water and land management, aridity detection, and climate projections, which helps farmers, resource managers, and locals improve irrigation water budgets, especially in areas facing water stress [2,10].

The most commonly used evapotranspiration determination methods are Thornthwaite [6], Blaney–Criddle [11], Jensen–Haise [12], and Hargreaves [13]. Other methods have also been used, such as Penman–Monteith, the Bioclimatic method of Alpat'eva, and the Bioclimatic method of G.K. Lgov [14,15]. Of the methods, while Penman–Monteith requires more complex data, Thornthwaite [6] and Hargreaves [13] use more limited and readily available data such as temperature, precipitation, and radiation [15–17].

AET was affected by several factors, including weather elements (radiation, air temperature, wind, humidity), soil properties (texture, structure, porosity, available water content), plant physiological characteristics (plant type, rooting depth, leaves, stomatal density), biomass (vegetation structure), and the environment [4,5,10]. Because determining the AET is complex, time-consuming, and only possible with sufficient weather stations, a common problem in developing and undeveloped countries, predicting/estimating and mapping the AET is crucial using readily available variables. Therefore, soil properties [18,19], weather [20–24], vegetation indices such as NDVI, EVI, and LAI [19,22,25–28], and topographical data [23,28] have been used as independent or proxy variables in predicting the AET. On the other hand, multilinear regression (MLR) [14,29,30], spline [15,31–36], IDW [37,38], KRIGING [30,31], and machine learning methods [39–41] are among the most used methods to predict the AET. Directly or indirectly using remote sensing to estimate the AET is another way that is popular among scientists [19,22,25,42,43]. Estimations' accuracy often depends on the methods used, the study area's characteristics (topography, vegetation cover), and the number of weather stations. In general, the accuracy levels improve from the simple estimation methods, such as MLR, to advanced methods, such as machine learning-remote sensing integration. Using MLR, Mardikis, Kalivas, and Kollias [30] and Güler [15] accounted for 37% to 74% and 59% to 90% of the variation in AET in Greece and Turkey, respectively. Combining machine learning and remote sensing methods, dos Santos, Mantovani, Fernandes, Filgueiras, Lourenco, Bufon, and Neale [40] and Wang, Wang, Ding, and Li [43] explained 80 to 91% and >85% of the variation in AET in Brazil and China, respectively. Hadadi, Moazenzadeh, and Mohammadi [19] also used remote sensing and artificial intelligence methods to predict AET, which reported relatively low errors (RMSE: 10.9 to 11.9 mm), including the soil wetness index, besides others (e.g., temperature, dew point, relative humidity, wind speed, sunshine hour, and vegetation indexes) in the model, reducing errors by 12.5 to 26.5%.

The research focused on Turkey as the study area, which is characterized by a limited number of weather stations due to political and economic challenges. Consequently, there is a demand for dependable and precise high-resolution climate surfaces crucial for global climate change monitoring and assessing meteorological disaster risks, encompassing temperature, precipitation, AET, and PET [44,45]. Some studies on estimating or interpolating evapotranspiration (AET, PET) have also been conducted in Turkey using different methodologies, such as random forests (RF), MLR, and artificial neural networks (ANN), with variable accuracies [46–49]. ANUSPLIN, an Australian National University spline-based program, was used in this study to interpolate the AET because of its numerous advantages, such as reducing the cross-validation error, considering the spatially changing climatic variables, and the effect of variable topography on the interpolation [34,50], and providing more accurate results with lower errors compared to other techniques such as IDW, OK (ordinary kriging), UK (universal kriging), CoKRG, and MLR [31]. In another group of studies, correlations between NDVI and AET/PET were examined, and significant relationships were reported [26,39].

Despite the critical importance of accurately estimating AET for effective water resource management, especially in regions with complex terrains like Turkey, there is a notable scarcity of studies employing advanced interpolation methods such as the ANUSPLIN model. Additionally, while the relationship between AET and vegetation indices like the NDVI has been explored in various contexts, comprehensive analyses integrating high-resolution spatiotemporal AET data with NDVI across diverse Turkish biomes remain limited. This study addresses these gaps by generating detailed AET surfaces using the ANUSPLIN model and examining their correlation with NDVI, thereby providing valuable insights for natural resource management in Turkey.

The present study aimed to (i) determine the terrestrial AET by region for the country using the Thornthwaite method, (ii) spatially interpolate the AET by ANUSPLIN and compare it at the regional level, and (iii) examine the relationships between the AET and NDVI across the country. Results from this study were analyzed and validated in three ways: (1) diagnostic statistics derived from a surface-fitting model, including signal, mean, root mean square predictive error (RTGCV), root mean square error estimate (RTMSE), root mean square residual of the spline (RTMSR), and calculation of the standard deviation of the noise in the spline (RTVAR). (2) error metrics between interpolated surfaces and calculated AET based on withholding 52 weather stations, such as adjusted coefficient of determination (R^2_{adj}), root mean square error (RMSE), mean absolute error (MAE), and bias (ME). (3) a comparison with other interpolation methods, such as IDW and KRG, using model performance metrics.

2. Materials and Methods

2.1. Study Area Description

Located between southeastern Europe and northeastern Asia, Turkey, the study area, has an area coverage of 780.580 square km (Figure 1) and is surrounded by the Mediterranean, Aegean, and Black Seas [51]. The country is geographically divided into seven regions: Central Anatolia (CA), Eastern Anatolia (EA), Black Sea (BS), Mediterranean (MED), Aegean (AEG), Southeastern Anatolia (SA), and Marmara (MAR). The elevation in the country averaged 1132 m, starting from sea level and reaching up to 5137 m in Mount Ararat [52]. Mountains and mountain ranges that rise from the western to the country's eastern regions and typically run parallel to the shore define the country's climate. Four main climate types are seen in the country: the humid temperate Black Sea, continental inland, Mediterranean, and Mediterranean-like climates, in which two factors dominate each, namely (1) different forms of weather and atmospheric disturbances from polar and tropical areas and (2) terrain, abrupt elevation changes, land-sea interactions, and thermodynamic effects [53]. The temperature averaged 13.5 °C (−2 °C in winter and 23 °C in summer), and precipitation averaged 628 mm, the lowest values in Konya and Igdir in Central and Eastern Anatolia, respectively, and the highest ones in Rize and Hopa on the coast of the Black Sea [54]. According to the IPCC, precipitation in most of the country is decreasing, and the temperature is increasing, parallel with global climate change due to interactions between the North Atlantic sector, continental Europe, and the Mediterranean Sea [55]. The variation in topography and climate dominates land use, land cover (LULC), and floristic diversity. Forests account for 27.6% of the total area, followed by agriculture (31.1%), rangeland (18.6%), wetland (1.1%), and others (artificial surfaces, bareland, artificial and semi-natural vegetation). The forested lands in the country cover 21.2 million ha, 53% of which is broadleaved, and 42% of which is conifers. The rest is mixed forest stands composed of conifer and broadleaved species [56,57].

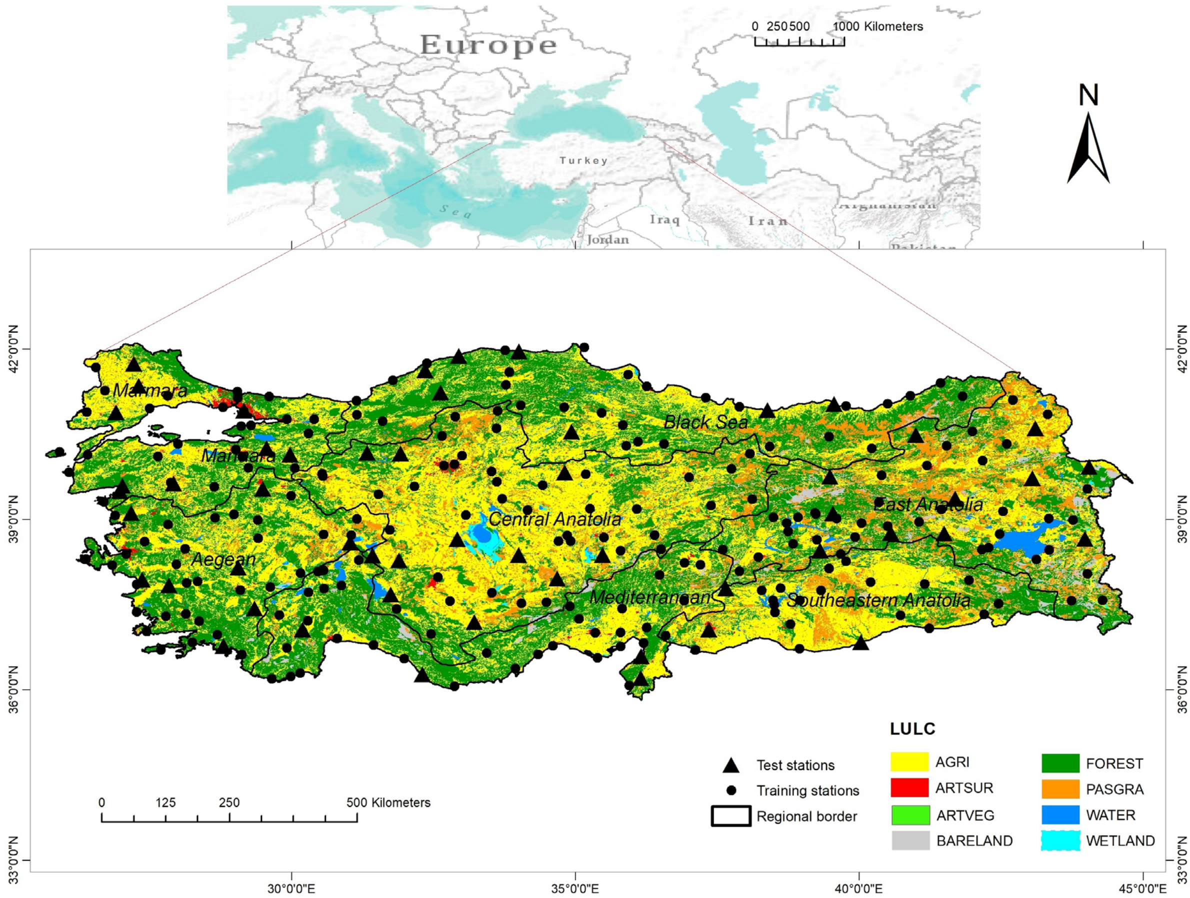

Figure 1. LULC map of the study area and locations of test and training weather stations. AGRI: Agriculture, ARTSUR: Artificial surfaces, ARTVEG: Artificial vegetation, PASGRA: Pasture and grasslands.

2.2. Data and Analysis

The flowchart showing the data collection, analysis, and methods used in the study is presented in Figure 2.

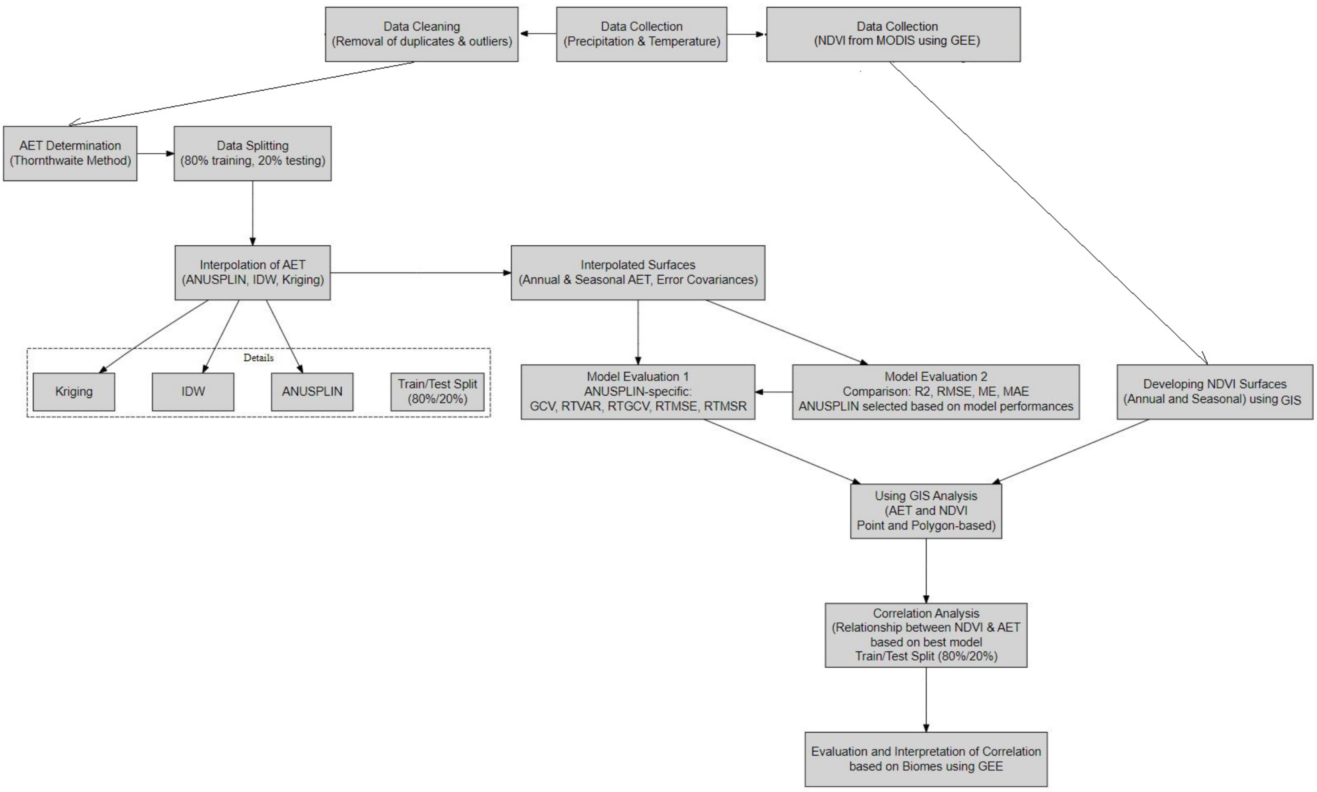

Figure 2. The flowchart showing the data collection, analysis, and methods used in the study (GCV: Generalized Cross Validation, RTVAR: Square Root of the Variance Estimate, RTGCV: Square Root of the Generalized Cross Validation, RTMSE: Square Root of the Mean Square Error, RTMSR: Square Root of the Mean Square Residual).

The long-term climate data to calculate AET consisted of mean annual temperature (MAT) and mean annual total precipitation (MATP) by month in 1960–2017, which were obtained from the Turkish State Meteorological Organization [58]. A thorough analysis has been conducted on the consistency and quality of long-term temperature and precipitation data derived from MGM [59–62]. The data were also checked for quality and duplication issues. A total of 20% of the data was used as a test, and the rest (80%) was utilized to train the model to ensure validation. Data selection for test and training datasets was randomly performed using SPSS 22.0. The elevation of weather stations was extracted from the DEM of the country [63]. The observation length of the stations varies slightly depending on the variables examined. Still, it may be broadly divided into four categories: less than 30 years (6.3–7.4%), between 30 and 40 years (8.1–8.5%), between 40 and 50 years (12.0–12.5%), and greater than 50 years (72.4–72.8%).

The Thornthwaite method was performed to determine AET, as reaching reliable spatial information about AET-related meteorological factors (e.g., surface humidity, solar radiation, and wind speed) is not easy [16]. To determine AET, first, Equation (1) was used.

$$PET = 16\left(\frac{10Ti}{I}\right)^{\alpha}[mm/month] \quad (1)$$

where PET indicates potential evapotranspiration, Ti is the monthly air temperature, and I is the annual heat index calculated using Equation (2). α is the complex function of heat index determined by Equation (3). The PET calculated is adjusted for day and month length using a correction factor based on the weather stations' latitudes [6].

$$I = \sum_{i=1}^{12} \left(\frac{Ti}{5}\right)^{1.514} \quad (2)$$

$$\alpha = 6.75 \times 10^{-7} I^3 - 7.71 \times 10^{-5} I^2 + 1.7912 \times 10^{-2} I + 0.49239 \quad (3)$$

After calculating the adjusted PET, AET is determined based on the following assumptions: (i) If monthly precipitation is greater than PET, then AET equals adjusted PET; (ii) if monthly precipitation is smaller than adjusted PET, then AET is the sum of monthly precipitation and water storage, based on the difference between precipitation and PET calculated by Equation (4); (iii) If the storage reduces to zero, AET equals monthly precipitation [64,65].

$$S_t = S_{t-1} + P_t - PET_t \quad (4)$$

where S_t is the soil water storage at the end of the month t, S_{t-1} indicates the soil water storage from the previous month, and P_t and PET_t represent the precipitation and PET in the month t, respectively. The deficit and surplus situations occur in the case of PET > precipitation and precipitation > PET, respectively, resulting in soil moisture reduction and surplussing of storage capacity, causing runoff.

The normalized difference vegetation index (NDVI) surfaces, indicating green plants' health and abundance within an area, were generated using the Google Earth Engine (GEE) platform for four seasons up to 2018. The spatial resolution of NDVI surfaces is 250 m, and the observation interval was 16 days. The images in this process use the blue band to remove residual atmosphere contamination caused by smoke and sub-pixel thin clouds, computed from atmospherically corrected bi-directional surface reflectance masked for water, clouds, aerosols, and cloud shadows [66].

The calculation of *NDVI* is as follows (Equation (5)), using spectral reflectance disparity between the red (*Red*) and near-infrared (*NIR*) bands of an image [67].

$$NDVI = (NIR - Red)/(NIR + Red) \quad (5)$$

Moreover, the distributional area of biomes to each geographical region and seasonal NDVI values for each biome were identified through world biomes' borders [68] extracted from GEE and seasonal NDVI maps developed for the current study to evaluate the spatiotemporal variation in NDVI. Accordingly, biomes were intersected with the regional border to determine the areal percentage of each region's biome type, and the average NDVI of each biome type in each season was calculated using the zonal statistics tool in ESRI's ArcMap 10.2.

2.3. Interpolation Methods

2.3.1. ANUSPLIN (Australian National University Spline)

ANUSPLIN 4.4, the package in Fortran language, authored by Hutchinson and Xu [69] and used for spatial interpolation of data (e.g., climate), employs a thin-plate smoothing spline (TPSS) algorithm to fit climate maps to noisy data using one or more explanatory variables. This technique performs better than other interpolation methods in complex terrains [45]. This software includes different tools such as Spline, Selnot, Addnot, Lapgrd, Lappnt, and Gcvgml. It typically uses cross-validation to give predicted climate data and its standard errors in point and grid format. Wahba [70,71] introduced TPSS, but Hutchinson [72] used it first to interpolate climate variables, creating ANUSPLIN.

Zi, indicating a corresponding variable (e.g., temperature, solar radiation, and relative humidity) given by Equation (6), is needed to interpret program outcomes regarding TPSS for N-measured data [69].

$$z_i = f(x_i) + b^T y_i + e_i(\beth = 1, \ldots, N) \tag{6}$$

where f represents an unknown and smooth function of the explanatory variables denoted as x_i, which may include factors like longitude and latitude. y_i signifies explanatory co-variates like elevation. b is used to represent the coefficient associated with y_i; e_i represents zero-mean random errors, accounting for measurement inaccuracies and insufficiencies within the TPSS model having the variance $wi\sigma^2$, where w_i and σ^2 are the relative error variance (known) and error variance (unknown), respectively. These variances remain constant across all data points [69,72]. The function f and the coefficient vector b are determined through the minimization of Equation (7).

$$\sum_{i=1}^{N} \left(\frac{z_i - f(x_i) - b^T y_i}{w_i} \right)^2 + \rho J_m(f) \tag{7}$$

Here, $J_m(f)$ serves as a measure of the complexity of f, and the "roughness penalty" is defined concerning an integral involving mth-order partial derivatives of f. On the other hand, p, a smoothing parameter, is shown with a positive number. The closer this value is to zero, the better the interpolant from the fitted function. If p tends towards infinity, the function f approaches a least squares polynomial.

The smoothing parameter selection typically involves minimizing the measured predictive error for the fitted surface, calculated using generalized cross-validation (GCV). In this process, GCV is determined by systematically excluding each data point, computing the residual from the omitted data point based on a surface fitted to all the other data points using the same p value. Equatiοn (8) quantifies the GCV for each value of p by summing up these squared residuals with appropriate weights [69,73].

$$GCV = \frac{\|W^{-1}(I - A)z\|^2 / N}{[tr(I - A)/N]^2} \tag{8}$$

A, I, and Tr $(I - A)$ in the above equation represent the identity matrix, influence matrix, and residual degrees of freedom. In contrast, Equation (9) calculates W, which is the diagonal matrix.

$$W = diag(\omega 1 \ldots \omega N) \tag{9}$$

The variance σ^2 of the data error e_i is calculated by Equation (10).

$$VAR = \frac{\|W^{-1}(I - A)z\|^2}{tr(I - A)} \tag{10}$$

The true mean square error of the fitted function (MSE) across the data points, the unbiased estimation, can be calculated by Equation (11), provided that the variance (σ^2) is either known or estimated.

$$MSE = \|W^{-1}(I - A)z\|^2 / N - 2\sigma^2 tr(I - A)/N + \sigma^2 \tag{11}$$

Craven and Wahba [74] have shown that under suitable conditions, the formula transformed into Equation (12);

$$GCV = MSE + \sigma^2 \tag{12}$$

The weighted mean residual sum of squares (MSR) is calculated using Equation (13).

$$MSR = \|W^{-1}(I - A)z\|^2 / N \tag{13}$$

The square roots of VAR (RTVAR), GCV (RTGCV), MSE (RTMSE), and MSR (RTMSR) are also calculated in the package and written to the output log files.

This study employed a second-order spline in combination with square root transformation for seasonal and annual AET, issued by Hutchinson and Xu [69], to mitigate the positive skewness of the data using ANUSPLIN version 4.4 with the SPLINE and LAPGRD tools.

Specifically, the SPLINE was used to fit a partial thin plate smoothing spline (TPSS) function to one or more independent variables, while the LAPGRD was utilized to calculate values and Bayesian standard error estimates of partial TPSS surfaces on a regular rectangular grid.

2.3.2. Inverse Distance Weighting (IDW)

IDW is one of the simplest and most widely used interpolation techniques. This method predicts unknown values at each point by computing the weighted mean of adjacent data points from the nearest 10–30 neighbors within a certain radius [75,76]. The approach is based on the assumption that values at closer locations are more similar to their values. Equation (14) is used to calculate the weighted means.

$$\lambda_i = \frac{\frac{1}{d_i p}}{\sum_{i=1}^{n} \frac{1}{d_i p}} \tag{14}$$

where d_i is the distance between points (x_0 and x_i), p is the power parameter (especially set to 2), an indicator for the accuracy, and n shows the number of points to be used for interpolation. The interpolation is considered local, not global, when p is greater than 2 [77].

2.3.3. Ordinary Kriging (KRG)

Unlike IDW, KRG uses a linear combination of weights at known points to predict values at unknown points [78,79].

KRG uses a geostatistical model (Equation (15)):

$$Z(s) = \mu + \varepsilon(s) \qquad s \in D \tag{15}$$

where μ represents the structural component of the field of interest, $\varepsilon(s)$ is the smooth variation plus measurement error, and D is the examination area.

The ordinary Kriging estimation is defined as a linear weighted average of the current number of observations (n), as indicated by Formula (16).

$$\hat{z}(s_0) = \sum_{i=1}^{n} \lambda_i z(s_i), \quad \sum_{i=1}^{n} \lambda = 1 \tag{16}$$

where $\hat{z}(s_0)$ is an estimate of KRG at s_0 location, $z(s_i)$ denotes the measured value at the known ith point (i = 1,. . ., n), n is the number of adjacent stations used to compute the interpolation, and $\lambda_{1,}$. . ., λ_n are weights based on the variogram [75].

2.4. Statistical Analyses and Evaluation of Model Performance

Point- and polygon-based approaches were followed to determine the associations between seasonal and annual NDVI and their corresponding AET across the country. About 7000 data points were randomly created and distributed over the study area using ArcMap for the point-based method, and 922 polygons (equaling each county in Turkey) were selected for the polygon-based approach. Then, AET and NDVI values for each point and polygon were extracted from the developed surfaces in ArcMap using the extract values to points and the zonal statistics tools. The statistics for AET and NDVI, such as minimum, maximum, and mean values for each geographical region, were computed also using zonal statistics tools. The regional statistical differences were tested using the Kruskal–Wallis test, the non-parametric equivalent of one-way ANOVA, and Dunn–Bonferroni tests for pairwise comparisons because of violations of parametric assumptions such as normal distribution and equality of variances [80]. Finally, the correlations with correlation coefficient, mean error, and mean absolute error between observed and predicted AET based on NDVI were determined and plotted for the test and training datasets using the SPSS Modeler 18.5 [81].

Model performances were evaluated using metrics such as R^2_{adj}, RMSE, MAE, and ME, calculated with Equations (17)–(20).

$$RMSE = \sqrt{\frac{1}{N}\sum_{i=1}^{N}(y_i - \hat{y})^2} \tag{17}$$

$$MAE = \frac{1}{N}\sum_{k=1}^{N}|y_i - \hat{y}| \tag{18}$$

$$R^2 = 1 - \frac{\sum(y_i - \hat{y})}{\sum(y_i - \overline{y})}, R^2_{adj} = 1 - \left(1 - R^2\right)\left[\frac{n-1}{n-(k+1)}\right] \tag{19}$$

$$ME = \frac{\sum_{i=1}^{N}(y_i - \hat{y})}{N} \tag{20}$$

where $\hat{y}$ is the predicted value of y, $\overline{y}$ is the mean value of y, n, and k are the number of observations and estimated parameters, respectively.

3. Results and Discussion

3.1. Spatiotemporal Interpolation by ANUSPLIN and Evaluation of Model Performance

Table 1 summarizes the regional variations in temperature and precipitation at annual and seasonal scales. Accordingly, the mean annual temperature (MAT) is 13.1 °C, ranging from 3.7 °C to 20.2 °C in the study area. Mean annual total precipitation (MATP) is 634.6 mm, with a minimum of 263.7 mm and a maximum of 2278.5 mm. Apparent regional disparities emerge as CA and BS exhibit the lowest and highest MATP at 422 mm and 854.7 mm, respectively. EA and MED, on the other hand, show the lowest and highest MAT at 9.6 °C and 17.0 °C, respectively.

National meteorological data from 274 stations also reveals distinct regional disparities in temperature and precipitation across seasons. During winter, the EA region experiences the country's coldest temperatures, plummeting to −6.5 °C. Conversely, summer brings scorching heat to the SA region, with recorded highs of 32.4 °C. Precipitation patterns also exhibit regional variations. The AEG region receives the least rainfall in summer, averaging a mere 2.4 mm, while autumn delivers the most abundant rain to the BS region, reaching a peak of 845.6 mm.

Leveraging the capabilities of ANUSPLIN's SPLINE and LAPGRD tools, a comprehensive analysis of interpolated actual evapotranspiration (AET) across Turkey for 1960–2017 was conducted. This investigation delved into seasonal variations and annual totals, generating detailed summary statistics presented in Table 2. The robust dataset employed encompassed data from randomly distributed 221 training (80%) and 53 test stations (20%), which enabled the construction of accurate seasonal (spring: AETspr, summer: AETsum, autumn: AETaut, and winter: AETwin) and annual (AETann) surfaces, along with their associated error covariances (standard errors) (Figures 3 and 4).

Table 1. Descriptive statistics for seasonal and annual temperature and precipitation by region obtained from 274 weather stations across the country from 1960 to 2017.

Region	Stat	Temperature (°C)					Precipitation (mm)				
		Spr	Sum	Aut	Win	Ann	Spr	Sum	Aut	Win	Ann
MED	Min	8.0	19.5	10.3	−0.2	8.8	85.7	11.0	73.7	128.3	375.2
	Max	18.5	28.2	22.5	14.8	20.2	339.6	106.4	293.9	627.7	1140.7
	Mean	14.7	25.2	17.9	9.0	16.3	179.7	41.8	164.4	332.4	726.2
EA	Min	2.5	14.5	5.4	−6.5	3.7	107.0	16.7	54.6	45.1	263.7
	Max	13.2	27.2	16.2	4.6	14.8	414.7	224.8	240.8	462.3	1166.0
	Mean	8.3	21.7	11.5	−0.6	9.6	215.5	56.9	129.7	182.0	582.4
AEG	Min	9.9	19.9	11.7	2.7	10.7	118.5	2.4	58.1	103.7	386.8
	Max	17.3	27.4	21.2	14.4	19.6	240.2	75.9	291.8	708.2	1258.4
	Mean	13.9	24.8	16.5	8.3	15.5	156.2	38.2	148.5	310.1	660.5
SE	Min	12.5	26.7	16.0	5.0	14.8	91.8	4.5	54.1	126.4	292.2
	Max	17.5	32.4	21.0	9.4	19.6	272.2	23.9	164.7	390.3	844.1
	Mean	15.0	29.2	18.5	7.1	17.0	178.2	13.0	110.3	245.2	566.6
CA	Min	6.1	17.3	8.2	−2.3	6.8	100.7	31.6	61.7	81.3	297.2
	Max	12.1	23.3	14.0	4.0	13.0	211.4	104.4	166.9	370.5	777.6
	Mean	9.8	20.7	11.8	1.9	10.6	142.6	56.8	87.7	135.0	422.0
BS	Min	6.3	16.4	8.9	−2.4	7.0	125.1	57.9	80.5	88.6	394.4
	Max	13.2	23.9	16.6	10.0	14.8	344.5	492.0	845.6	711.1	2278.5
	Mean	11.1	21.1	14.0	6.0	12.6	185.6	161.3	262.1	273.1	854.7
MAR	Min	3.3	13.3	6.5	−1.1	5.1	115.3	21.8	104.2	144.9	461.4
	Max	14.9	25.9	17.6	10.3	16.6	403.4	172.7	351.0	554.1	1464.4
	Mean	12.1	22.6	15.0	7.1	13.8	164.8	82.2	193.5	278.1	707.2
Country	Min	2.5	13.3	5.4	−6.5	3.7	85.7	2.4	54.1	45.1	263.7
	Max	18.5	32.4	22.5	14.8	20.2	414.7	492.0	845.6	711.1	2278.5
	Mean	11.7	23.1	14.5	5.0	13.1	174.5	65.4	153.7	242.6	634.6

Table 2. Diagnostic metrics for seasonal AET (mm) surfaces generated by ANUSPLIN across the country.

Seasons	Signal Ratio	Min.	Max.	Mean	SD.	SE	RTGCV	RTMSE	RTMSR	RTVAR	*p*
Spring	0.58	21.12	204.00	133.70	25.54	0.80	3.15	1.55	1.31	1.96	0.01
Summer	0.45	5.42	503.90	141.80	68.1	3.01	11.87	5.90	6.56	1.54	0.02
Autumn	0.68	35.56	193.30	81.49	34.7	1.39	5.66	2.64	1.82	1.34	0.05
Winter	0.52	0.00	74.00	10.51	20.94	0.70	2.77	1.38	1.32	0.64	0.01
Annual	0.54	225.90	755.30	364.30	93.99	3.69	14.52	7.24	6.71	2.74	0.01

SD: standard deviation; SE: standard error; RTGCV: root means predictive error; RTMSE: root mean square error estimate; RTMSR: root mean square residual of the spline; RTVAR: standard deviation of the noise in the spline.

Table 2 provided insights into the spatial and temporal variability of AET across Turkey. The annual average AET is 364.3 ± 23.3 mm, with considerable spatial variability ranging from 225.9 ± 18.6 mm to 755.3 ± 35.8 mm, which is consistent with the findings reported by Bölük [64].

Winter is the season with the lowest average AET at 10.5 ± 2.5 mm, exhibiting further extremes up to 74.5 ± 9.5 mm. Conversely, summer reigns supreme in terms of AET, boasting an average of 141.8 ± 22 mm and a more comprehensive range spanning 5.4 ± 4.6 mm to 510.2 ± 56.7 mm. Based on the average AET from the regions by season (Table 3, Figure 5), the highest AETann was observed in BS (453.1 ± 26.2 mm) and MAR (436.2 ± 25.5 mm), followed by decreasing order through MED (369.3 ± 23.4 mm), AEG (366.3 ± 22.9 mm), CA (330.8 ± 22 mm), EA (329.5 ± 22.4 mm), reaching the lowest value in SE (295.7 ± 20.9 mm) ($p < 0.001$). The highest seasonal AET values by region were observed in SE during spring (157 ± 5.0 mm), BS during summer (224.8 ± 28.5 mm), MAR during autumn (116.5 ± 9.1 mm), and winter (26.2 ± 5 mm). Similar results were reported in other studies in Algeria and India [29,82,83], attributing the higher AET to abundant precipitation and dense vegetation in northern parts compared to southern ones.

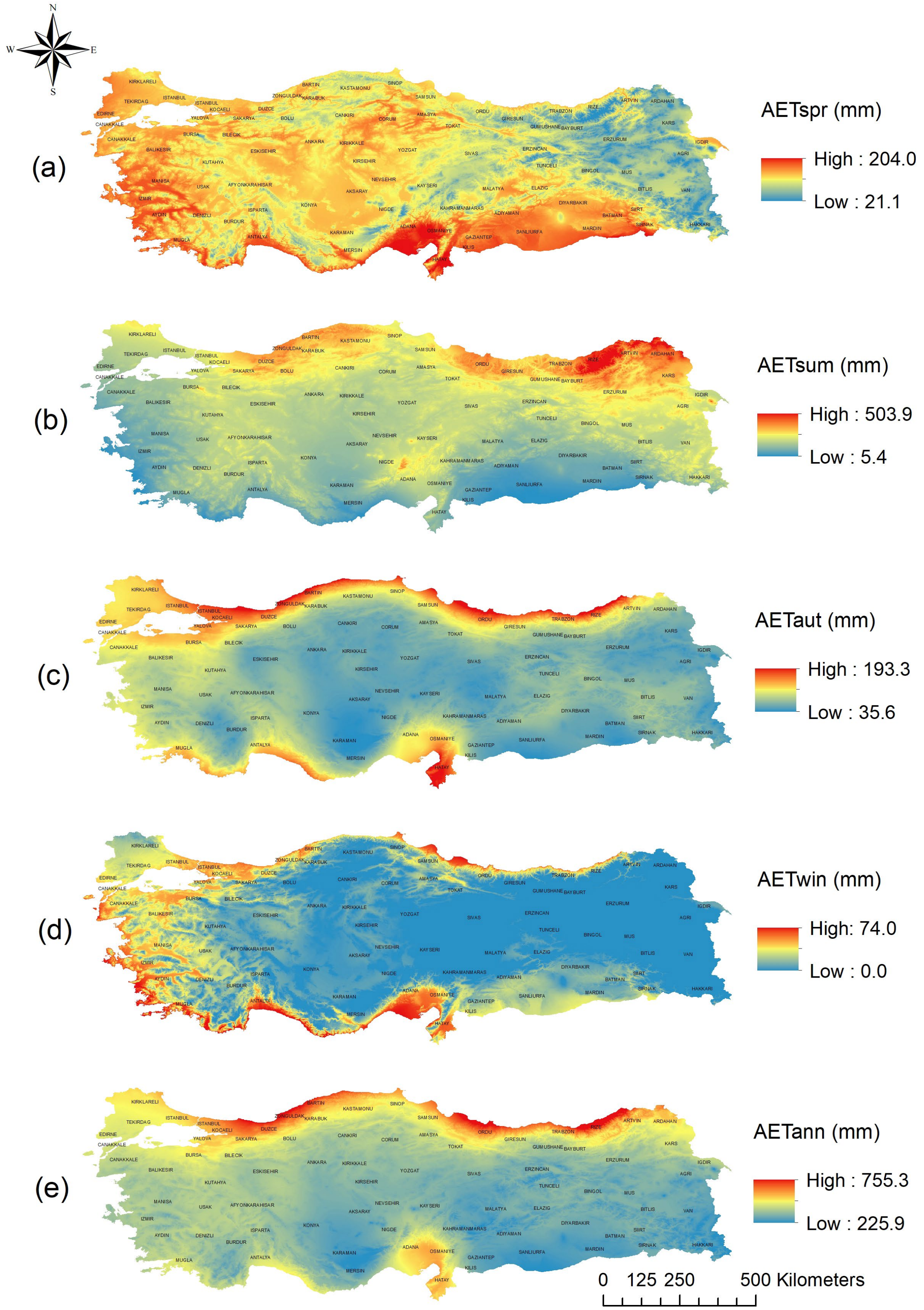

Figure 3. The interpolated AET surfaces by season for Turkey ((**a**): spring, (**b**): summer, (**c**): autumn, (**d**): winter, (**e**): annual).

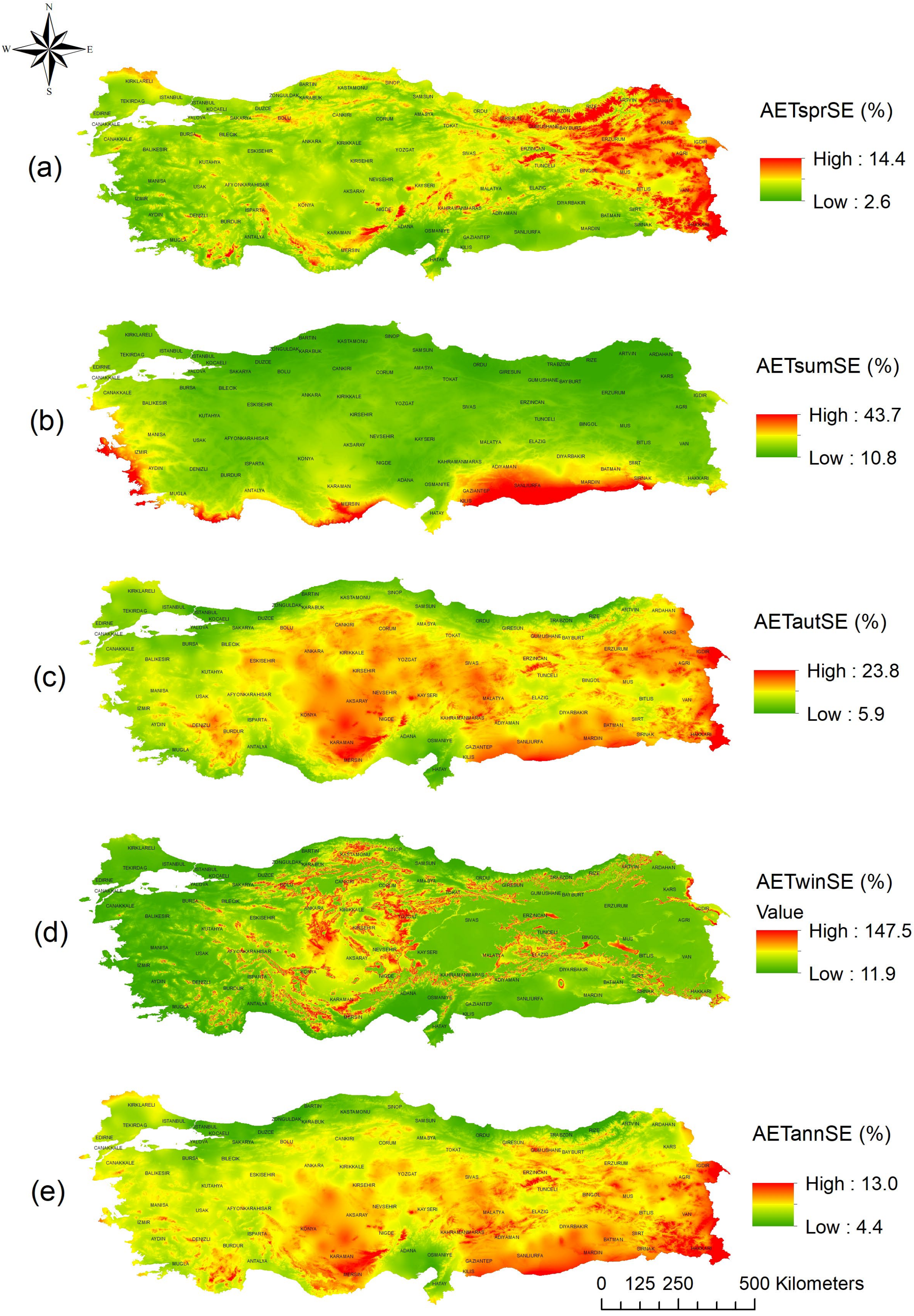

Figure 4. The surfaces for standard error of interpolated AET by season ((**a**): spring, (**b**): summer, (**c**): autumn, (**d**): winter, (**e**): annual).

Table 3. Descriptive statistics regarding predicted AET with SE by geographical region.

Region	Statistic	AETspr	AETsum	AETaut	AETwin	AETann
AEG	Min	82.7 ± 3.9	5.7 ± 4.7	51.7 ± 6	0 ± 0.2	295 ± 21.4
	Max	192.3 ± 6.3	215.2 ± 29.6	141.9 ± 10.7	74.3 ± 9.4	434.1 ± 26.7
	Mean	151.2 ± 4.9 ^{a}	102.6 ± 18.4 ^{a}	86.3 ± 7.6 ^{a}	21.6 ± 4.2 ^{a}	366.3 ± 22.9 ^{a}
BS	Min	34.9 ± 3.3	115 ± 19.6	54.5 ± 6.2	0 ± 0.2	297.3 ± 21.1
	Max	176.1 ± 5.7	510.2 ± 56.6	193.3 ± 12.5	58 ± 8	755.3 ± 35.8
	Mean	126.3 ± 4.6 ^{b}	224.8 ± 28.5 ^{b}	102 ± 8.5 ^{b}	10 ± 2.5 ^{b}	453.1 ± 26.2 ^{b}
CA	Min	47.5 ± 3.5	36.7 ± 11.5	40 ± 5.5	0 ± 0.2	242.5 ± 19.5
	Max	182.1 ± 5.5	300 ± 41.1	105.7 ± 9.1	35.9 ± 6	454 ± 27.8
	Mean	134.2 ± 4.6 ^{c}	133.9 ± 21.6 ^{c}	63.8 ± 6.6 ^{c}	3.1 ± 1.4 ^{c}	330.8 ± 22 ^{c}
EA	Min	21.1 ± 2.9	60.4 ± 14.6	35.6 ± 5.8	0 ± 0.2	225.9 ± 19.5
	Max	166.7 ± 7	473.7 ± 55.3	122.3 ± 11.1	13.3 ± 5	583.3 ± 34.7
	Mean	101.1 ± 4.1 ^{d}	173.5 ± 25 ^{d}	67.7 ± 7 ^{d}	0.4 ± 0.4 ^{d}	329.5 ± 22.4 ^{d}
MAR	Min	69.8 ± 3.6	47.2 ± 12.9	63.7 ± 6.6	0 ± 0.2	324.5 ± 22.1
	Max	176.7 ± 6.6	299 ± 34.5	183.1 ± 13.3	56.9 ± 8.2	646.1 ± 34.2
	Mean	148.6 ± 4.9 ^{a}	142 ± 22.3 ^{c}	116.5 ± 9.1 ^{e}	26.2 ± 5 ^{e}	436.2 ± 25.5 ^{b}
MED	Min	55.7 ± 3.5	15.8 ± 7.6	43.9 ± 5.8	0 ± 0.2	237.6 ± 19.5
	Max	204 ± 6.7	301.2 ± 41.2	181.8 ± 13.8	71.5 ± 9.2	532.7 ± 33
	Mean	145.8 ± 4.9 ^{e}	106.4 ± 19.1 ^{a}	92.6 ± 8 ^{a}	18 ± 3.5 ^{f}	369.3 ± 23.4 ^{e}
SE	Min	56.1 ± 3.5	8.5 ± 6	47.4 ± 5.7	0 ± 0.2	252 ± 18.5
	Max	201.8 ± 6.2	198.6 ± 30.7	134.5 ± 10.4	33.9 ± 6.1	426.5 ± 26.4
	Mean	157 ± 5 ^{f}	58.8 ± 13.9 ^{e}	66 ± 6.8 ^{f}	11.4 ± 3.1 ^{f}	295.7 ± 20.9 ^{f}
Country	Min	21.1 ± 2.9	5.7 ± 4.6	35.6 ± 5.6	0 ± 0.2	225.9 ± 18.6
	Max	201.8 ± 7.2	510.2 ± 56.7	193.3 ± 13.9	74.3 ± 9.5	755.3 ± 35.8
	Mean	133.7 ± 4.7	141.8 ± 22	81.5 ± 7.5	10.5 ± 2.5	364.3 ± 23.3

Different Superscripted lower-case letters attached to mean values indicate significant regional differences according to the Dunn–Bonferroni test following the Kruskal–Wallis test. MAR: Marmara, AEG: Aegean, BS: Black Sea, CA: Central Anatolia, EA: Eastern Anatolia, MED: Mediterranean, SE: Southeastern Anatolia. Spr: spring, Sum: summer, Aut: autumn, Win: winter, Ann: annual.

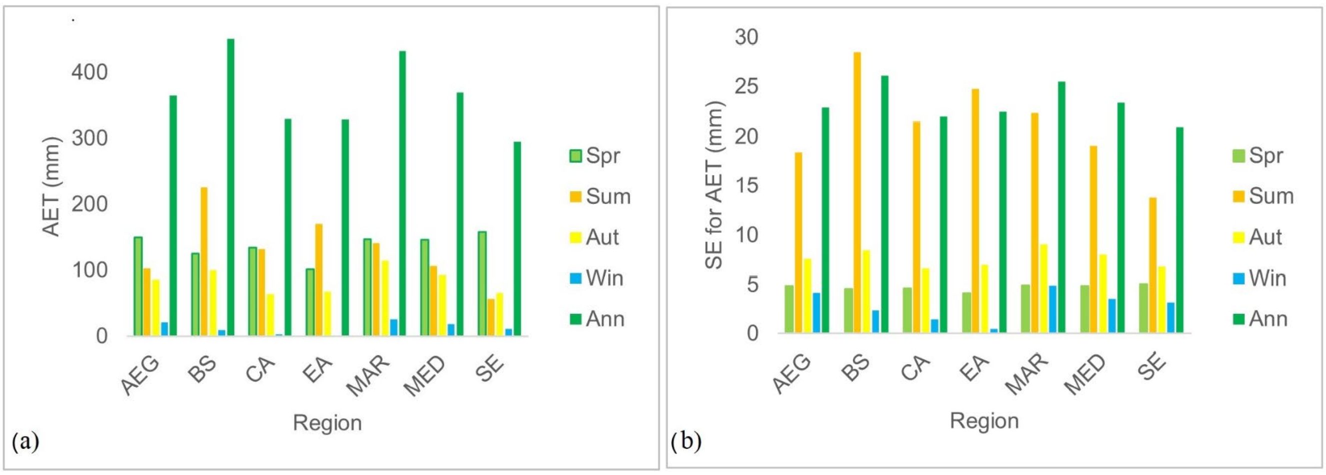

Figure 5. The distribution of AET (**a**) and error covariance of AET (**b**) to the region by season. MAR: Marmara, AEG: Aegean, BS: Black Sea, CA: Central Anatolia, EA: Eastern Anatolia, MED: Mediterranean, SE: Southeastern Anatolia. Spr: spring, Sum: summer, Aut: autumn, Win: winter, Ann: annual.

This spatial variation in AET, under the control of regional LULC, aligns with the results of Dong, Hu, Wei, Liu, Xu, Yan, Chen, Li, and Khan [18] and Yao et al. [84], who reported a decreasing trend in AET from evergreen forests to sparsely vegetated or barren lands. This pattern was attributed to the processes of transpiration and evaporation, hydrothermal conditions, and vegetation changes.

Spring and summer contributed more to the annual AET, accounting for 75% of the total (Spr: 36.4% and Sum: 38.6%), followed by AETaut (22.2%) and AETwin (2.9%). Jian et al. [85] also found similar contributions of seasons to the AETann (AETsum: 114.8 mm, AETspr: 42 mm, and AETaut: 21.8 mm) in the Tarim River Basin, China. AET reached its annual minimum during winter. The combined influence of plant dormancy and reduced soil water evaporation primarily drives this decline. When most plants wilt and transpiration nearly ceases, only weak evaporation from soil moisture sustains AET at this low level. Spring, however, brings a dramatic reversal. Increased precipitation and rising temperatures foster the return of vibrant vegetation. Transpiration is rapidly amplified as plants resume their active water exchange. Simultaneously, the warming soil contributes to an enhanced rate of evaporation. This potent synergy triggers a gradual yet substantial ascent in AET, marking spring as a period of revitalized water loss from plant and soil surfaces [43].

The average AETann covariance error exhibited considerable variability, ranging from 4.4% to 13.0%, with an average of 6.5% across the country. This variability manifested seasonally, with AETspr and AETaut exhibiting the lowest average error of 9.7% (range: 2.7–14.4% and 5.9–23.8%) and AETwin the highest at 36.0% (range: 11.9–147.5%), followed by AETsum (average: 17.6%, range: 10.8–43.7%) (Figure 4, Table 3).

The spatial (regional) and temporal (seasonal) variability in the error covariances of AET fluctuated depending on the topography, which controls the climatic parameters shaping vegetation cover. The models performed worst in predominantly mountainous regions of BS and EA during spring, likely due to lower temperatures and NDVI values.

Similarly, in SE, MED, and AEG during summer, errors were probably related to insufficient soil water retention, exacerbated by higher temperatures and reduced rainfall. In autumn, central regions like CA, EA, and SE, relatively far from the sea and characterized by sparse vegetation and low precipitation, showed significant errors, particularly in the mountainous areas of EA and CA, where temperatures remained relatively low (Table 1, Figures 6 and 7).

These spatial and temporal variations in model performance highlight the critical role of climatic conditions, such as precipitation, temperature, vegetation cover, and soil moisture, influencing AET estimations. Previous research has shown that AET accuracy improves in densely vegetated areas compared to sparsely vegetated regions [25,43,86]. In China, the correlation between NDVI and AET was reported as $r = 0.67$ [28] and $r = 0.87$ [22]. Furthermore, the effects of precipitation ($r = 0.66$) and temperature ($r = 0.93$) on the AET model precision were demonstrated by Ling, Yang, Xu, Yu, Xia, and Guo [22], who also proved the soil wetness index's effects on the model precision, reducing the estimation errors by 12.5 to 26.5%, underscoring its importance in regions with complex topography. On the other hand, the spatial patterns of annual AET and its error covariance in the present study resemble those of annual precipitation and its error surfaces presented by Yener [87] for Turkey, which shows higher interpolation error could be attributed to scarce weather stations in mountainous parts of the regions such as the Black Sea and Eastern Anatolia. Wu, Liu, and Xing [33] and Wang, Sun, Li, and Luo [32] also attributed significant prediction errors, especially in mountainous regions in Anhui province and the Yellow River basin in China, to scarce weather stations.

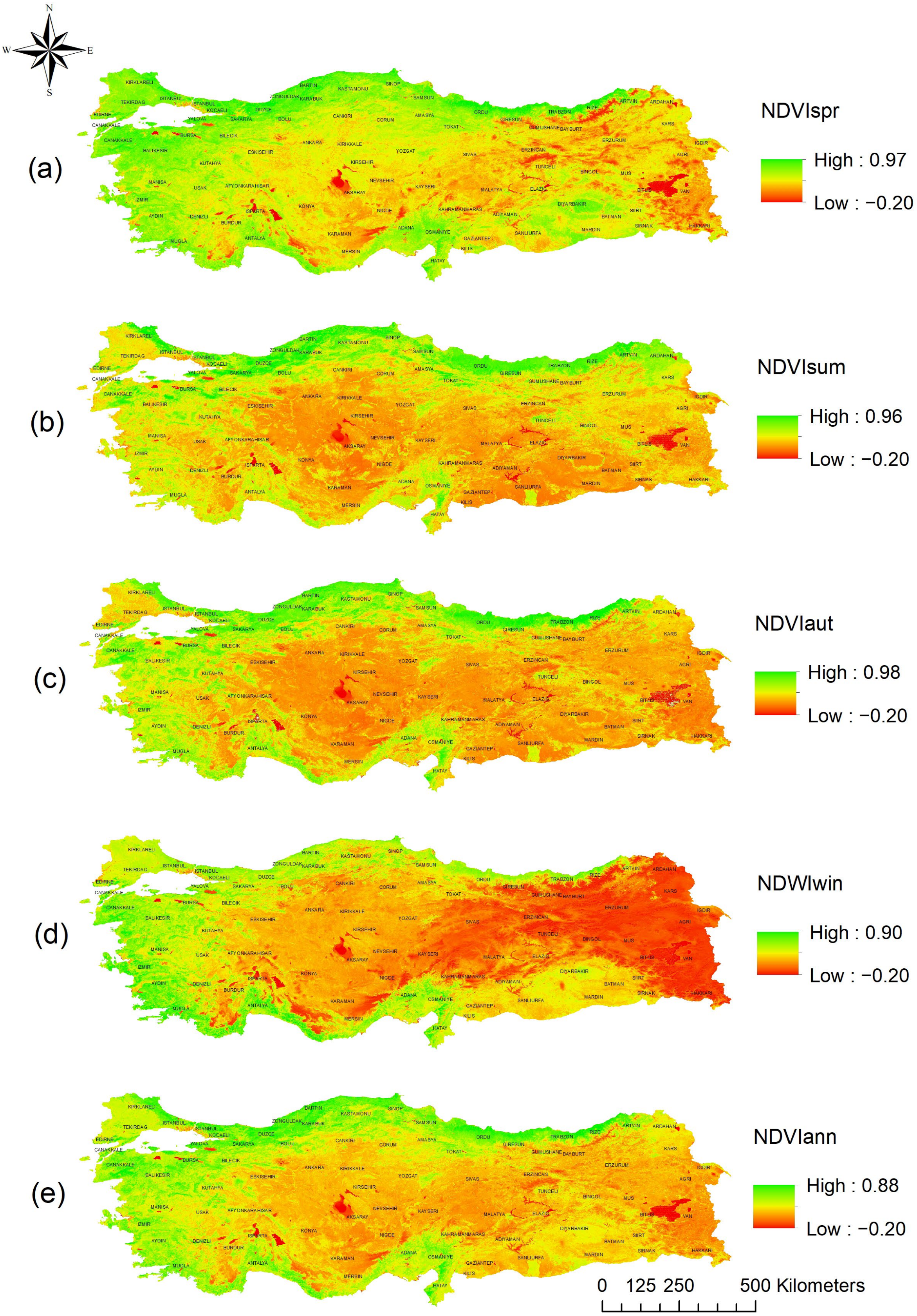

Figure 6. Average NDVI by season for Turkey ((**a**): spring, (**b**): summer, (**c**): autumn, (**d**): winter, (**e**): annual).

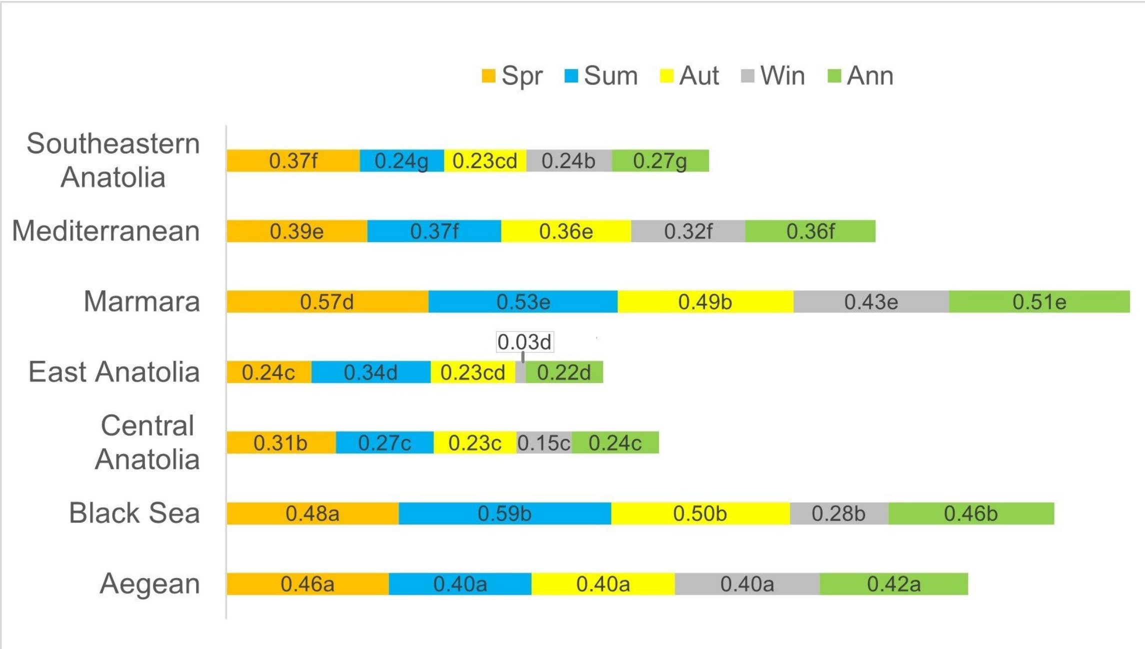

Figure 7. Average seasonal and annual NDVI by geographical regions (Spr: spring, Sum: summer, autumn: Aut, Win: winter, Ann: annual.). Colors represent the seasons and annual values: orange for spring, blue for summer, yellow for autumn, gray for winter, and green for annual. Different lower-case letters attached to mean NDVI values indicate significant differences by region according to the Dunn–Bonferroni test following the Kruskal–Wallis test.

However, ANUSPLIN outperformed most studies with fewer errors than other methods because it considers the spatial variability in topography using all data points [34,88].

This study optimized the seasonal and annual AET interpolation by employing some diagnostic statistics (Table 2) proposed by Hutchinson and Xu [69] to evaluate interpolation performance, such as p, signal ratio, RTGCV, and RTMSE. The smoothing parameter (p) had a specific range (0.01–0.02), slightly adjusting to $p = 0.05$ for autumn. This approach balanced model flexibility, allowing it to adapt to seasonal variations while minimizing the overfitting issue. The model's degrees of freedom, represented by the signal ratio, ranged from 0.45 to 0.68 throughout the year. These values, around half the number of weather stations, suggest an appropriate balance between model complexity and data accuracy, the proof of capturing spatial variations without overfitting or losing sight of the actual data. Robust performance metrics like RTGCV (2.77–11.87 mm annually) and RTMSE (1.38–5.90 mm annually) further confirmed the model's effectiveness and accuracy in capturing spatial AET variations throughout the year. This study successfully characterized nationwide seasonal and annual AET variations by prioritizing model fit and data accuracy. This study employed a high-resolution spatial grid of 0.005° (~600 m) to generate seasonal and annual AET surfaces. The selection of spatial resolution is significant for capturing climatic characteristics, particularly in regions with complex terrain like Turkey [89]. The resolution suggests fine detail compared to other studies using the ANUSPLIN model. For instance, Zhao, Li, Yang, Tang, Yin, Luan, and Sun [34] and Wang, Wang, Ding, and Li [43] employed a 5 km resolution for their AET maps in China. Even AET maps with coarser resolutions were developed in studies such as Tait and Woods [31], using a ~6 km resolution for New Zealand. The resolution in interpolation studies utilizing other methods ranged from coarser, e.g., 9.3 km for Columbia [39], moderate, e.g., ~1 km for the Tibetan Plateau with an area of 2.5 million km^2 [90], to finer, e.g., 30 m for the Colorado River Basin with an area of 630,000 km^2 [91].

3.2. Validation and Comparison

Model validation was tested with error metrics such as R^2_{adj}, RMSE, MAE, and ME (detailed in Table 4), computed using differences between fitted surfaces and withholding data, which was 20% of all weather stations. These metrics were also used to compare ANUSPLIN-fitted surfaces with others, such as IDW and KRG.

Table 4. Comparison of interpolation techniques with error metrics between observed and predicted AET (mm) for the test dataset.

Method		**ANUSPLIN**				**IDW**				**KRG**			
Season	Mean	RMSE	MAE	ME	R^2_{adj}	RMSE	MAE	ME	R^2_{adj}	RMSE	MAE	ME	R^2_{adj}
Spring	150.7	**5.56**	4.12	0.90	**0.93**	10.29	7.81	1.37	0.77	10.90	8.23	1.38	0.75
Summer	127.1	**33.14**	22.94	−2.14	**0.73**	36.25	23.87	−1.80	0.69	34.32	22.77	−3.27	0.72
Autumn	93.9	**10.50**	8.06	0.33	**0.91**	17.77	12.12	0.19	0.75	26.04	17.96	1.98	0.46
Winter	20.1	**4.33**	2.90	0.19	**0.94**	8.02	5.35	−0.61	0.81	9.60	6.42	−0.39	0.72
Annual	391.7	**39.35**	26.77	−2.72	**0.83**	52.20	30.88	−0.86	0.71	68.91	42.34	3.01	0.49

RMSE: Root mean squared error, MAE: Mean absolute error, ME: Mean error or bias, R^2_{adj}: Adjusted coefficient of determination. The bold values indicate that the performance criteria are superior to other methods.

The models' fit was adequate according to model metrics. The ANUSPLIN-fitted surfaces accounted for the variation in AET by annually 83% with an RMSE of 39.35 mm and seasonally ranged from 73% in summer with an RMSE of 33.14 mm to 94% in winter with an RMSE of 4.33 mm. The seasonal bias (ME), which was relatively small and ranged between −2.14 mm (underestimation) and 0.90 mm (overestimation), also supported the models' adequacy, compared to IDW (annual: −0.86 mm, seasonal: −1.80–1.37 mm) and KRG (annual: 3.01 mm, seasonal: −3.27–1.38 mm).

These performance metrics are consistent with the previous studies using the ANUSPLIN model [28,31,32,34,43,92,93] at various scales and capturing the variation in evapotranspiration (AET, PET) at variable rates. For instance, Tait and Woods [31] interpolated the PET over New Zealand using ANUSPLIN with a resolution of 0.05°, which resulted in lower errors and more accuracy in complex terrain, minimizing the GCV [34], with RMSE ranging from 0.4 mm in winter to 1 mm in summer. Similarly, Wang, Sun, Li, and Luo [32] and Wang, Luo, Shafeeque, Zhou, and Li [28] interpolated the monthly PET over the Yellow River Basin, China, having an area of 774,700 km^2, with an RMSE of 6.5–7.9 mm. The PET decreased from SE to NW in the region because the SE was dominated by dense vegetation like forests, which consume more water than other land-use types. On the other hand, Rigden and Salvucci [93] interpolated the ET with the RMSE, ranging from 87 to 125 mm/year, over America, using four different methods and 305 weather station data. Another study [91] interpolating the AET in the Colorado River Basin, USA, determined the bias and R^2_{adj} to be between −16 and 22 mm and 0.52 and 0.88 in the study where they interpolated the AET in the Colorado River basin using MODIS and Landsat-based image combinations.

In this study, IDW and KRG techniques exhibited lower performance than ANUSPLIN. R^2_{adj} was 0.71 and 0.49 annually; seasonally, it ranged from 0.69 to 0.81 and 0.46 to 0.75 for IDW and KRG, respectively. Their annual RMSE was 52.20 mm and 68.91 mm and seasonally ranged from 8.02 to 36.25 mm and 9.6 to 34.32 mm for IDW and KRG, respectively, which suggests that although both interpolation techniques captured general trends, the models' precision in estimating particular data points was less consistent than that of ANUSPLIN. Several climate-related studies, including those by Basconcillo et al. [94] in the Philippines and Zhao, Huang, Xie, Wu, Xie, Feng, and Chen [89] in the Tibetan Plateau, reported better interpolation performance with ANUSPLIN than with others such as IDW and KRG, since ANUSPLIN, using the longitude and latitude as independent and elevation as a covariate, captured the variation in AET.

Various studies have also been implemented to interpolate/predict and map evapotranspiration over the world [19,22,40,95,96] using different methods except ANUSPLIN and comparing them with others.

Several studies performed in Turkey employed topographic (LAT, LONG, ELEV) and climatic (temperature, solar radiation, relative humidity, and wind speed) data as predictors to estimate and map the ET using various techniques except ANUSPLIN, such as MLR, RF, support vector regression (SVR), extreme machine learning (EML), ANN, adaptive network-based fuzzy inference system (ANFIS), and the METRIC method, satellite-based mapping evapotranspiration at high resolution and with internalized calibration. Among these, the ANFIS model achieved the highest accuracy ($R^2{}_{adj}$ = 0.98, RMSE = 0.2 mm) [48], followed by ANN ($R^2{}_{adj}$ = 0.94–0.97, RMSE = 0.4–15.6 mm) [49,97,98], EML ($R^2{}_{adj}$ = 0.95, RMSE = 1.15 mm) [46], and METRIC ($R^2{}_{adj}$ = 0.63–0.98, RMSE = 0.6–1.2 mm) [99]. The achievements of methods with the best accuracies could be attributed to considering the nonlinear relations [46]. Another example [15] of interpolating ET in the central Black Sea, Turkey, used 72 weather stations' data employing several methods such as MLR, Kriging (simple, ordinary, universal), spline, and IDW, and the MLR outperformed.

The studies performed abroad using other methods (random forest, nearest neighbor, local average) besides IDW and KRG yielded different results. For example, the survey conducted in northeast Brazil by da Silva Júnior, Medeiros, Garrozi, Montenegro, and Gonçalves [37] found the RF with 0.93 to 0.96 $R^2{}_{adj}$ and 1.64% RMSE to be the best-performing method to interpolate ET; the nearest neighbor method was found to be superior in Oklahoma with a coefficient of determination of 0.98 in Walsh, Solie, and Raun's [38] study. Mardikis, Kalivas, and Kollias [30] used MLR, gradient-plus, GIDS, and RK, besides the abovementioned techniques, to interpolate ET and GIDS, and RK outperformed with an MAE of 0.124 to 0.160 mm/day.

3.3. Spatiotemporal Variation in NDVI and Its Relationship with AET

3.3.1. Spatiotemporal Variation in NDVI

Figures 6 and 7 demonstrate the spatial and temporal variability of NDVI throughout Turkey. The annual average NDVI with standard deviation is 0.33 ± 0.16, ranging from −0.20 to 0.88, indicating significant spatial heterogeneity, and considering the temporal variability, summer and spring exhibit the highest average NDVI (0.38 ± 0.19 and 0.38 ± 0.16), followed by autumn (0.33 ± 0.17) and winter (0.23 ± 0.18), which aligns with the AET (Figure 3, Table 3). Figure 7 shows the regional variations of NDVI. MAR had the highest annual average NDVI with 0.51, followed by BS (0.46), AEG (0.42), MED (0.36), SA (0.27), CA (0.24), and EA (0.22), whose NDVI was the lowest. The average NDVI reaches peak values mostly in summer and spring, ranging between 0.24–0.59 and 0.24–0.48, respectively, and the lowest value mostly in winter, ranging from 0.15 to 0.40. Notably, the spatial variations by season align with the AET trends (Figures 3 and 5) with minor discrepancies. Some studies also found similar seasonal trends to those in the present study, indicating the most NDVI in the growing season, followed by autumn and winter.

Vegetation has numerous vital roles in terrestrial ecosystems' biogeochemical cycles, energy exchange, and water balance, and therefore, global climate change and NDVI represent the trend of vegetation growth. The main driver of NDVI fluctuations is climate (e.g., rainfall and temperature), followed by land cover and others (e.g., population) [100–103]. For example, the study performed by Yang, Wang, Bai, Tan, Li, Wu, Tian, Hu, Li, and Deng [100] over the world implied a negative correlation between NDVI and temperature in relatively arid regions and positive correlations in mostly subhumid or humid areas worldwide. The decreasing trend in NDVI with elevated temperature is attributed to increased soil evaporation, causing disruptions in photosynthesis. Unlike these relations, NDVI increased with abundant rainfall in dry areas, improving plant growth, and decreased in relatively moist regions, in which abundant rainfall causes increased cloud cover, reduced incident radiation, and increased soil moisture, negatively affecting plant growth [104].

Because the biome types are closely related to climate, the spatiotemporal variation in NDVI values was also evaluated in light of biomes in the study area. Accordingly, four distinct biomes were identified in the country according to Dinerstein, Olson, Joshi, Vynne, Burgess, Wikramanayake, Hahn, Palminteri, Hedao, Noss, Hansen, Locke, Ellis, Jones, Barber, Hayes, Kormos, Martin, Crist, Sechrest, Price, Baillie, Weeden, Suckling, Davis, Sizer, Moore, Thau, Birch, Potapov, Turubanova, Tyukavina, de Souza, Pintea, Brito, Llewellyn, Miller, Patzelt, Ghazanfar, Timberlake, Klöser, Shennan-Farpón, Kindt, Lillesø, van Breugel, Graudal, Voge, Al-Shammari, and Saleem [68], with the following percentage areas: Temperate Broadleaf and Mixed Forests (BROADMIXED, 39.1%), Mediterranean Forests, Woodlands, and Scrub (MEDFOR, 34.4%), Temperate Grasslands, Savannas, and Shrublands (TEMPGRASS, 13.5%), and Temperate Conifer Forests (TEMPCONFOR, 13.0%).

Figure 8a highlighted that the MEDFOR biome predominates in four regions (SE, MED, MAR, AEG). The regions CA and EA were dominated by the BROADMIXED biome and TEMPGRASS biome, respectively. However, the region BS was dominated nearly equally by BROADMIXED and TEMPCONFOR biomes. Except for the winter season, there is an order for the regions MAR/BS > AEG > MED > SE > EA/CA regarding NDVI. MAR exhibits higher NDVI values than BS in the spring and for the whole year. In contrast, the BS surpasses the MAR during summer and autumn. In the winter, the order changed most entirely as follows: MAR > AEG > MED > BS > SE > EA > CA because of the decreased temperature and its growth-reducing effect. The higher NDVI in the MAR than that of the BS region in the spring, winter, and annually could be attributed to relatively higher temperature-promoting physiological processes in plants and, thus, higher growth and longer growing seasons [105]. This spatiotemporal NDVI variation could be linked to the dominant biome types in the regions (Figure 8a,b). Namely, while the MEDFOR biome dominates the MAR region, the BS is dominated by the TEMPCONFOR biome.

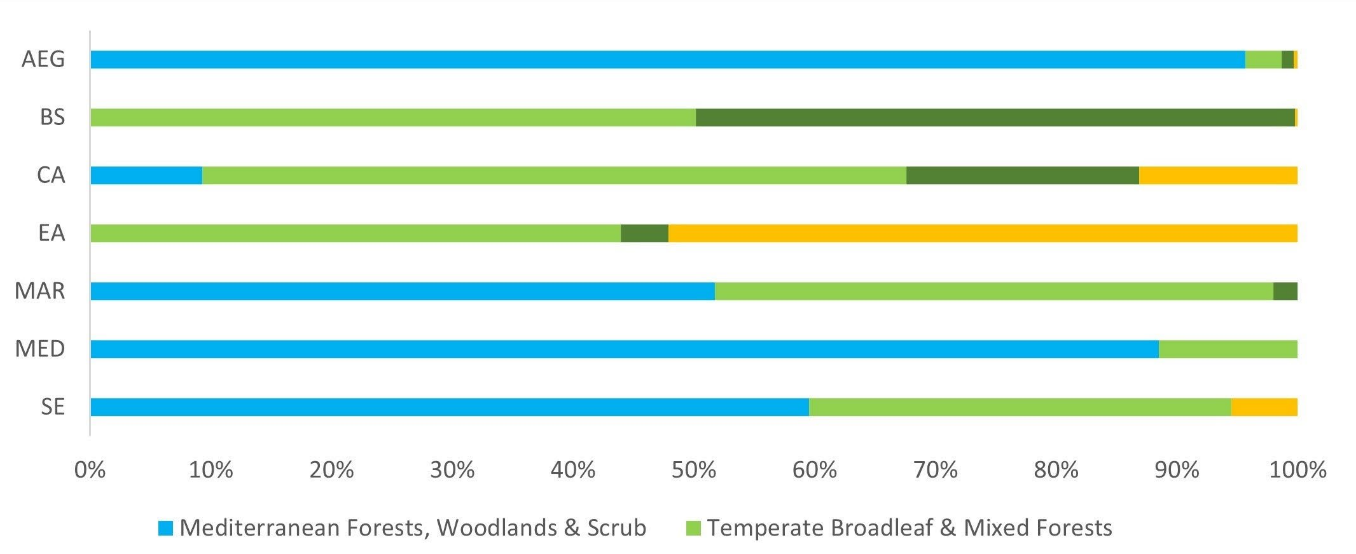

(a)

Figure 8. *Cont*.

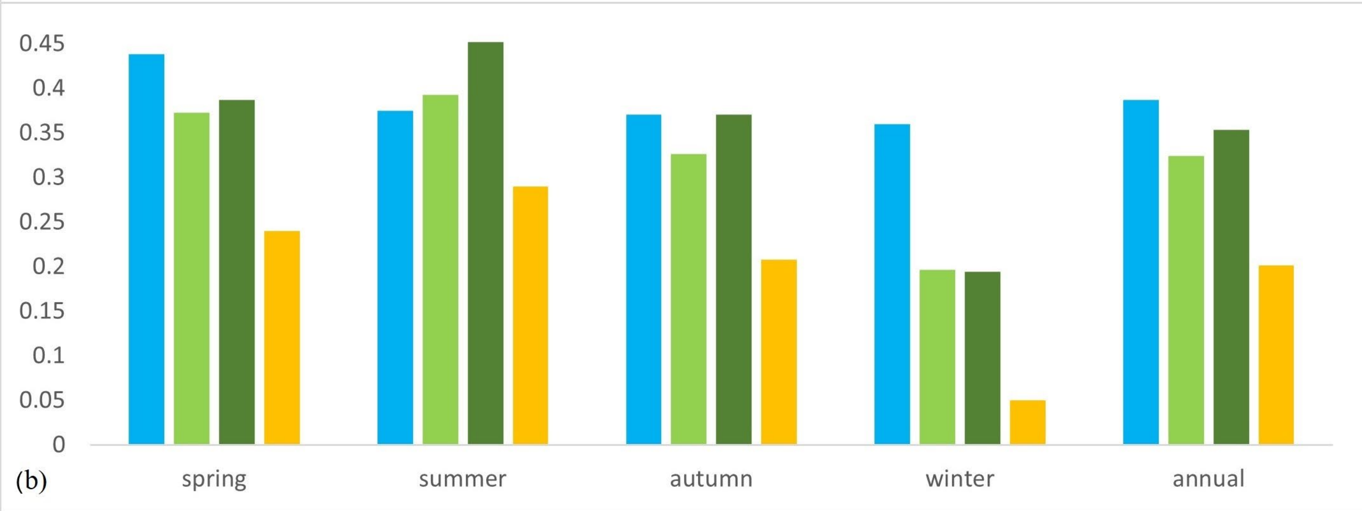

Figure 8. Areal distribution of biome types (**a**) and average seasonal NDVI values by biome (**b**) across regions.

Ergüner et al. [106] and Aktürk [107] attributed the highest NDVI value in the regions dominated by the MEDFOR biome to optimal rainfall and temperature conditions and available soil water capacity (AWC), especially in growing seasons, supporting plant growth. The regions CA and EA experienced the lowest NDVI values in almost all seasons, which are dominated by or include TEMPGRASS and BROADMIXED biomes characterized by relatively low rainfall and high temperatures and thus low AWC in the growing season (Table 1) [106].

Considering the weights of biomes in each region and looking at the seasonal NDVI values distribution by region (Figure 8a), it is noticed that it fits Figure 8b, showing seasonal NDVI values of each biome.

3.3.2. NDVI—AET Relations

Figures 9 and 10 summarized the correlations between NDVI and AET, validating them with test data and performance metrics (r, ME, and MAE for point- and polygon-based data).

The correlation coefficient between seasonal NDVI and AET showed variations, ranging from 0.49 in summer to 0.71 in winter for point-based data and 0.62 in spring to 0.83 in autumn and winter for polygon-based test data. Similarly, the MAE trended seasonally, changing from 14.0% in spring to 68.2% in winter for point-based and 9.6% in spring to 33.7% in winter for polygon-based test data. Unlike the seasonal relations, the annual relations between AET and NDVI data were more accurate, as evidenced by higher r (0.67 to 0.86) and lower MAE (8.5 to 11.4%). The outperforming of the polygon-based (Figure 10) to the point-based (Figure 9) method in determining spatial relations was evidenced and discussed by Zhan et al. [108] and Visztra et al. [109].

The relationship between AET and NDVI is reciprocal, complex, and essential for understanding water cycles and plant dynamics [110], which means rising AET through enhanced temperature, especially in semiarid and arid areas, reduces plant growth and increases mortality, evidenced by Vatandaslar et al. [111], reporting Taurus fir mortality in the Central Mediterranean region of Turkey because of increases in AET together with reductions in precipitation; conversely, denser vegetation causes rising AET through enhanced transpiration [112]. The effect of changing AET on NDVI is also manifested in other ways. AET plays a role in supporting plant growth by impacting soil moisture levels. Limited soil moisture may, therefore, harm vegetation [83]. Thus, AET plays a pivotal role in vegetation management [113]. For example, Arast et al. [20] reported a corresponding enhancement in vegetation associated with higher AET using time series analysis. While an increase in AET corresponds to greater biomass captured by elevated NDVI, a reduction, on the contrary, may result in a decline in plant health reflected by lower NDVI values [114]. Therefore, it has been the subject of numerous studies [20,28,95,96,115–120]

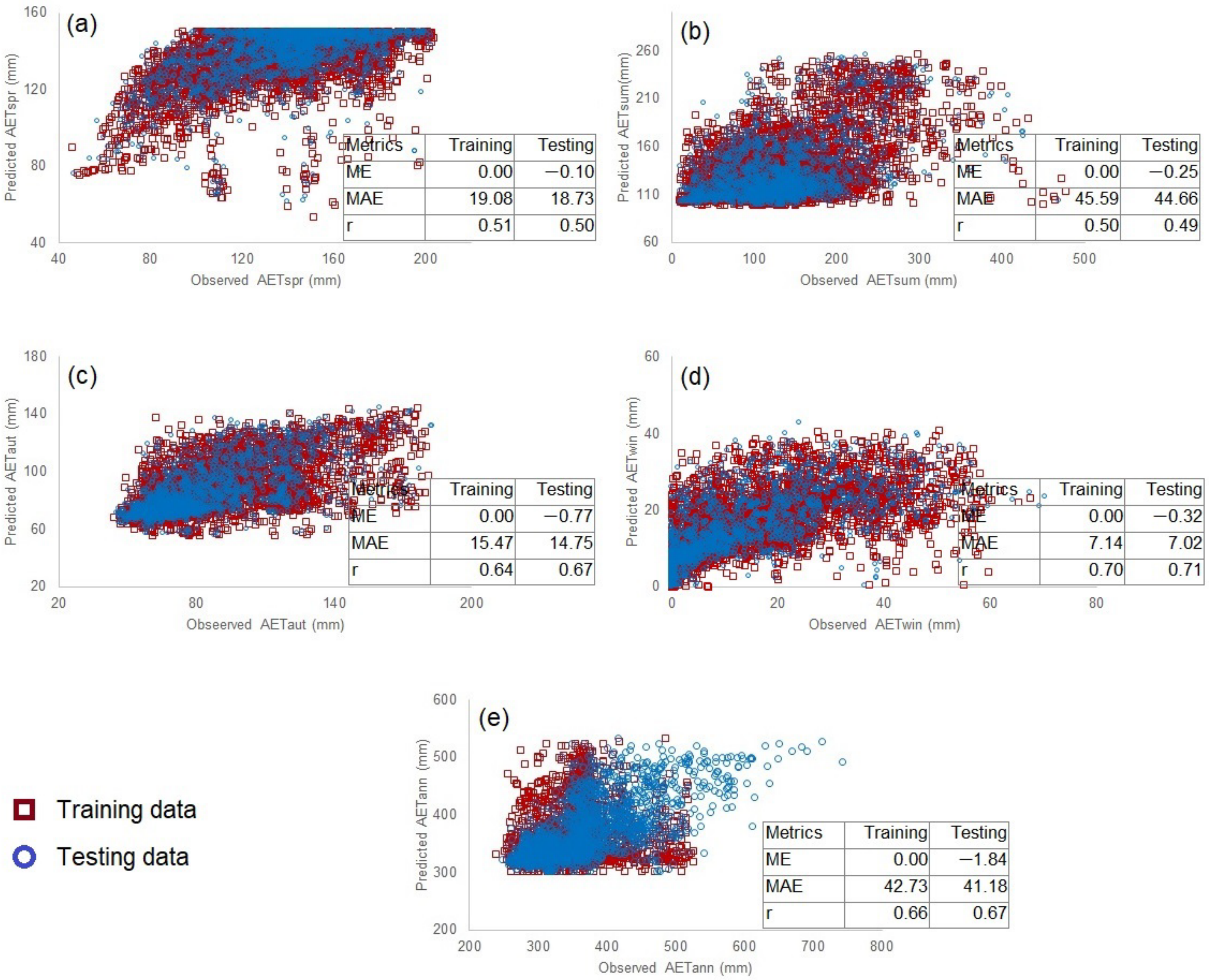

Figure 9. Correlation between NDVI-based predicted and observed AET using point data ((**a**): spring, (**b**): summer, (**c**): autumn, (**d**): winter, (**e**): annual).

These studies across diverse regions have consistently shown that NDVI, as a proxy for vegetation health and density, is closely related to AET, especially in drier seasons and climates [20]. This relationship is often modulated by precipitation, temperature, soil moisture, land cover, and topography [99]. The magnitude of the relationship between these two components is related to the presence or absence of moisture alongside others (statistical and analyzing methods used and the previously mentioned modulators), meaning strong relations in subhumid and humid and weak ties in semiarid and arid regions.

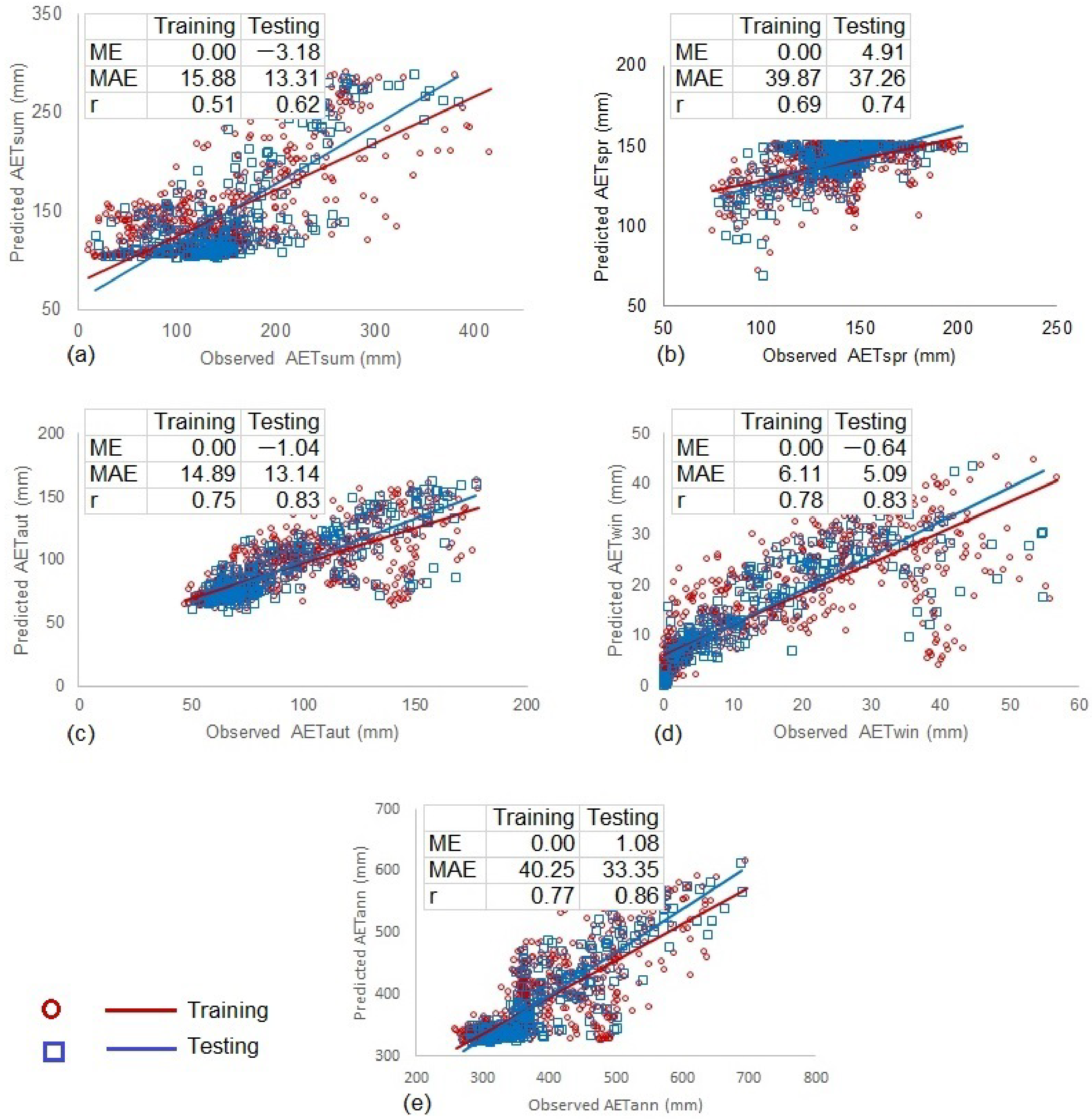

Figure 10. Correlation between NDVI-based predicted and observed AET using polygon data ((**a**): summer, (**b**): spring, (**c**): autumn, (**d**): winter, (**e**): annual).

For example, NDVI explained 50–52% of the variation in AET in semiarid grasslands [110] and 81% in subhumid and humid areas of Colombia [39]. Ling, Yang, Xu, Yu, Xia, and Guo [22] noted similar positive correlations (r = 0.74) between NDVI and AET, also having solid correlations with temperature (r = 0.87) and precipitation (r = 0.63) in the Yiluo River Basin of China, which suggests higher AET because of higher NDVI due to dense upstream vegetation, abundant rainfall, and sufficient energy for evaporation [85]. The close NDVI-AET relations (r = 0.38 to 0.59) in forested lands of Brazil were attributed to the effect of temperature and soil water besides rainfall and the difference between rainfall falling on the ground and used by vegetation [120,121]. Jaramillo et al. [122] attributed the increasing AET to enhanced transpiration (surface water evaporation) depending on the forest enhancement. The water evaporated through transpiration also changes by forest stand types (e.g., species traits) besides LULC. For example, while spruce stands intercepted and evaporated 20.6% of open area precipitation in Czechia, beech stands intercepted and evaporated 7.8%, attributing higher stem flow of beech (18.8%) than spruce (1.4%) [123].

4. Conclusions

Turkey's diverse and complex physiography leads to significant climate variability, which requires sufficient observation networks. However, many regions, especially those far from industrialized areas, lack adequate meteorological stations, which makes it challenging to collect reliable weather data, stressing the necessity for robust spatiotemporal climate models to predict variables such as precipitation, temperature, and evapotranspiration. This study aimed to spatiotemporally interpolate and evaluate seasonal and annual variations in AET across Turkey, focusing on geographical regions using the ANUSPLIN model. ANUSPLIN is particularly effective in areas with sparse weather stations, intricate terrain, and sharp elevation changes. Additionally, this study analyzed the spatiotemporal patterns of regional NDVI and its relationship with AET, considering topography, climate, and biome types.

To achieve this, data from 274 weather stations, with 20% withheld for model testing, were used to generate seasonal and annual AET surfaces through ANUSPLIN. This method produced more accurate estimates than other interpolation techniques, such as IDW and Kriging, as evidenced by performance metrics, including signal ratio, RTGCV, RTMSE, and RTVAR. Five high-resolution AET surfaces (0.005°, equivalent to about 0.6 km) were created: one for each season and one for the entire year.

The analysis of AET's spatiotemporal behavior showed that average seasonal AET decreased in the order of spring > summer > autumn > winter, corresponding to variations in precipitation and temperature, which also affected vegetation conditions. Regional AET variability was similarly influenced, with coastal areas—characterized by higher rainfall and temperatures and, therefore, more vegetation—exhibiting higher AET values. In contrast, the interior regions, which are more arid and semiarid with lower precipitation and temperature, showed lower AET values. Model performance was closely tied to rainfall, temperature, and vegetation cover, with higher accuracy in areas with ample rainfall and vegetation, which support the necessary heat flux for AET processes. Model performance was lower in mountainous regions such as the BS and EA, where lower temperatures and NDVI were observed. Similarly, the country's inner parts, such as EA, SE, and CA, exhibited reduced AET due to colder temperatures and sparse vegetation. Overall, the model performed best in spring, summer, and autumn, with the poorest performance in winter. It achieved its highest accuracy in regions with abundant precipitation and vegetation, such as BS and MAR. It performed worst in SE and EA, with minimal rainfall and vegetation.

This study also highlighted the significant influence of vegetation cover on AET, reflected in both direct correlations and regional variations. In contrast, higher maximum temperatures during summer, particularly in regions like SE, MED, and AEG, led to drought conditions due to insufficient soil moisture, reducing both AET values and model performance. NDVI patterns corresponded with biome types shaped by climate variation, revealing that the TEMPCONFOR and BROADMIXED biomes dominate the humid and subhumid regions, such as BS. In contrast, MEDFOR biomes are more prevalent in arid and semiarid areas, such as the Mediterranean MED and MAR regions. Abundant rainfall generally results in higher NDVI values, except in winter when temperature becomes a more dominant factor than rainfall (as seen in BS vs. MAR).

Despite the strong performance of the models, this study is limited by the geographical scope and the lack of predictive accuracy in certain areas, particularly mountainous regions in the BS, EA, and MED. The scarcity of weather stations in these areas also impacts the accuracy of the results. Future studies would pool data from additional weather stations and satellite imagery and employ additional vegetation indices like NDVI, EVI, and SAVI as independent variables for modeling and mapping AET. Incorporating mobile weather stations could further improve accuracy.

Funding: This research received no external funding.

Institutional Review Board Statement: Not applicable.

Informed Consent Statement: Not applicable.

Data Availability Statement: Data are contained within the article.

Acknowledgments: I would like to thank Can Vatandaslar for his valuable proofreading and the Turkish State Meteorological Service for providing data. Additionally, I would like to acknowledge the contributions of the reviewers and the journal editors to improve the manuscript.

Conflicts of Interest: The author declares no conflicts of interest.

References

1. Dong, Q.; Zhan, C.; Wang, H.; Wang, F.; Zhu, M. A review on evapotranspiration data assimilation based on hydrological models. *J. Geogr. Sci.* **2016**, *26*, 230–242. [CrossRef]
2. Wang, H.; Jia, G. Regional estimates of evapotranspiration over Northern China using a remote-sensing-based triangle interpolation method. *Adv. Atmos. Sci.* **2013**, *30*, 1479–1490. [CrossRef]
3. Türkeş, M. *General Climatology: The Principles of Air and Climate (In Turkish: Genel Klimatoloji: Atmosfer, Hava ve Iklimin Temelleri)*; Kriter Yayınları: Istanbul, Turkey, 2016.
4. Matin, M.; Bourque, C.P.A. Influence of vegetation cover on regional evapotranspiration in semi-arid watersheds in northwest China. In *Evapotranspiration—An Overview*; IntechOpen: London, UK, 2013.
5. Jovanovic, N.; Israel, S. Critical review of methods for the estimation of actual evapotranspiration in hydrological models. In *Evapotranspiration—Remote Sensing and Modeling*; IntechOpen: London, UK, 2012.
6. Thornthwaite, C.W. An approach toward a rational classification of climate. *Geogr. Rev.* **1948**, *38*, 55–94. [CrossRef]
7. Meentemeyer, V. Macroclimate the Lignin Control of Litter Decomposition Rates. *Ecology* **1978**, *59*, 465–472. [CrossRef]
8. Liski, J.; Nissinen, A.R.I.; Erhard, M.; Taskinen, O. Climatic effects on litter decomposition from arctic tundra to tropical rainforest. *Global Change Biol.* **2003**, *9*, 575–584. [CrossRef]
9. Jovanovic, N.Z.; Bugan, R.D.H.; Israel, S. Quantifying the evapotranspiration component of the water balance of Atlantis Sand Plain Fynbos (South Africa). In *Evapotranspiration—An Overview*; IntechOpen: London, UK, 2013; pp. 39–59.
10. Hart, Q.J.; Brugnach, M.; Temesgen, B.; Rueda, C.; Ustin, S.L.; Frame, K. Daily reference evapotranspiration for California using satellite imagery and weather station measurement interpolation. *Civ. Eng. Environ. Syst.* **2009**, *26*, 19–33. [CrossRef]
11. Blaney, H.F. Determining Water Requirements in Irrigated Areas from Climatological and Irrigation Data; 1952. Available online: https://ia600207.us.archive.org/1/items/determiningwater96blan/determiningwater96blan.pdf (accessed on 9 September 2024).
12. Jensen, M.E.; Haise, H.R. Estimating evapotranspiration from solar radiation. *J. Irrig. Drain. Div.* **1963**, *89*, 15–41. [CrossRef]
13. Cuenca, R.H.; Nicholson, M.T. Application of Penman Equation Wind Function. *J. Irrig. Drain. Div.* **1982**, *108*. [CrossRef]
14. Esin, A.I.; Solovyev, D.A.; Kamyshova, G.N.; Terekhova, N.N.; Korsaka, V.V. Evapotranspiration prediction based on chebyshev interpolation. *Int. Trans. J. Eng. Manag. Appl. Sci. Technol.* **2019**, *10*, 10.
15. Güler, M. A Comparison of Different Interpolation Methods Using the Geographical Information System for the Production of Reference Evapotranspiration Maps in Turkey. *J. Meteorol. Soc. Jpn. Ser. II* **2014**, *92*, 227–240. [CrossRef]
16. Xu, H.-j.; Wang, X.-p.; Zhao, C.-y. Drought sensitivity of vegetation photosynthesis along the aridity gradient in northern China. *Int. J. Appl. Earth Obs. Geoinf.* **2021**, *102*, 102418. [CrossRef]
17. Nistor, M.M.; Rai, P.K.; Carebia, I.A.; Singh, P.; Pratap Shahi, A.; Mishra, V.N. Comparison of the effectiveness of two Budyko-based methods for actual evapotranspiration in Uttar Pradesh, India. *Geogr. Tech.* **2020**, *15*, 1–15. [CrossRef]
18. Dong, Z.Q.; Hu, H.C.; Wei, Z.W.; Liu, Y.P.; Xu, H.L.; Yan, H.; Chen, L.J.; Li, H.Q.; Khan, M.Y.A. Estimating the Actual Evapotranspiration of Different Vegetation Types Based on Root Distribution Functions. *Front. Earth Sci.* **2022**, *10*, 893388. [CrossRef]
19. Hadadi, F.; Moazenzadeh, R.; Mohammadi, B. Estimation of actual evapotranspiration: A novel hybrid method based on remote sensing and artificial intelligence. *J. Hydrol.* **2022**, *609*, 127774. [CrossRef]
20. Arast, M.; Ranjbar, A.; Mousavi, S.H.; Abdollahi, K. Assessment of the Relationship Between NDVI-Based Actual Evapotranspiration by SEBS. *Iran. J. Sci. Technol. Trans. A-Sci.* **2020**, *44*, 1051–1062. [CrossRef]
21. Kosa, P. The effect of temperature on actual evapotranspiration based on Landsat 5 TM Satellite Imagery. *Evapotranspiration* **2011**, *56*, 209–228.

22. Ling, M.H.; Yang, Y.Q.; Xu, C.Y.; Yu, L.L.; Xia, Q.Y.; Guo, X.M. Temporal and Spatial Variation Characteristics of Actual Evapotranspiration in the Yiluo River Basin Based on the Priestley-Taylor Jet Propulsion Laboratory Model. *Appl. Sci.* **2022**, *12*, 9784. [CrossRef]
23. Mensah, F.O.; Alo, C.A. Modeling monthly actual evapotranspiration: An application of geographically weighted regression technique in the Passaic River Basin. *J. Water Clim. Change* **2023**, *14*, 17–37. [CrossRef]
24. Yang, L.S.; Feng, Q.; Zhu, M.; Wang, L.M.; Alizadeh, M.R.; Adamowski, J.F.; Wen, X.H.; Yin, Z.L. Variation in actual evapotranspiration and its ties to climate change and vegetation dynamics in northwest China. *J. Hydrol.* **2022**, *607*, 127533. [CrossRef]
25. Abbasi, N.; Nouri, H.; Didan, K.; Barreto-Munoz, A.; Borujeni, S.C.; Opp, C.; Nagler, P.; Thenkabail, P.S.; Siebert, S. Mapping Vegetation Index-Derived Actual Evapotranspiration across Croplands Using the Google Earth Engine Platform. *Remote Sens.* **2023**, *15*, 1017. [CrossRef]
26. Drerup, P.; Brueck, H.; Eticha, D.; Scherer, H.W. NDVI-based estimates of evapotranspiration of winter wheat indicate positive effects of N fertilizer application on agronomic water-use efficiency. *J. Agron. Crop Sci.* **2020**, *206*, 1–12. [CrossRef]
27. Gwate, O.; Mantel, S.K.; Finca, A.; Gibson, L.A.; Munch, Z.; Palmer, A.R. Estimating evapotranspiration in semi-arid rangelands. *Afr. J. Range Forage Sci.* **2019**, *36*, 17–25. [CrossRef]
28. Wang, Y.Q.; Luo, Y.; Shafeeque, M.; Zhou, M.L.; Li, H.Y. Modelling interannual variations in catchment evapotranspiration considering vegetation and climate seasonality using the Budyko framework. *Hydrol. Process.* **2021**, *35*, e14118. [CrossRef]
29. Aieb, A.; Kadri, I.; Lefsih, K.; Madani, K. Spatiotemporal trend analysis of runoff and actual evapotranspiration in Northern Algeria between 1901 and 2020. *Model. Earth Syst. Environ.* **2022**, *8*, 5251–5267. [CrossRef]
30. Mardikis, M.G.; Kalivas, D.P.; Kollias, V.J. Comparison of Interpolation Methods for the Prediction of Reference Evapotranspiration—An Application in Greece. *Water Resour. Manag.* **2005**, *19*, 251–278. [CrossRef]
31. Tait, A.; Woods, R. Spatial Interpolation of Daily Potential Evapotranspiration for New Zealand Using a Spline Model. *J. Hydrometeorol.* **2007**, *8*, 430–438. [CrossRef]
32. Wang, Y.; Sun, L.; Li, H.; Luo, Y. Monthly/8-km Grid Meteorological Dataset at the Middle and Upper Reaches of the Yellow River Basin of China (1980–2015). *J. Glob. Change Data Discov.* **2022**, *6*, 25–36. [CrossRef]
33. Wu, R.; Liu, Y.; Xing, X. Evaluation of evapotranspiration deficit index for agricultural drought monitoring in North China. *J. Hydrol.* **2021**, *596*, 126057. [CrossRef]
34. Zhao, J.; Li, C.; Yang, T.; Tang, Y.; Yin, Y.; Luan, X.; Sun, S. Estimation of high spatiotemporal resolution actual evapotranspiration by combining the SWH model with the METRIC model. *J. Hydrol.* **2020**, *586*, 124883. [CrossRef]
35. Nistor, M.M.; Satyanaga, A.; Dezsi, S.; Haidu, I. European Grid Dataset of Actual Evapotranspiration, Water Availability and Effective Precipitation. *Atmosphere* **2022**, *13*, 772. [CrossRef]
36. Zhang, X.; Kang, S.; Zhang, L.; Liu, J. Spatial variation of climatology monthly crop reference evapotranspiration and sensitivity coefficients in Shiyang river basin of northwest China. *Agric. Water Manag.* **2010**, *97*, 1506–1516. [CrossRef]
37. da Silva Júnior, J.C.; Medeiros, V.; Garrozi, C.; Montenegro, A.; Gonçalves, G.E. Random forest techniques for spatial interpolation of evapotranspiration data from Brazilian's Northeast. *Comput. Electron. Agric.* **2019**, *166*, 105017. [CrossRef]
38. Walsh, O.S.; Solie, J.B.; Raun, W.R. Can Oklahoma Mesonet Cumulative Evapotranspiration Data Be Accurately Predicted Using Three Interpolation Methods? *Commun. Soil Sci. Plant Anal.* **2013**, *44*, 892–899. [CrossRef]
39. Arbelaez, C.J.G.; Ramirez, A.G.; Giraldo, N.R.; Hernandez, J.D.R. Evapotranspiration Estimated in Colombia Using NDVI Data and Neural Networks. Available online: https://www.proceedings.com/content/030/030674webtoc.pdf (accessed on 9 September 2024).
40. dos Santos, R.A.; Mantovani, E.C.; Fernandes, E.I.; Filgueiras, R.; Lourenco, R.D.; Bufon, V.B.; Neale, C.M.U. Modeling Actual Evapotranspiration with MSI-Sentinel Images and Machine Learning Algorithms. *Atmosphere* **2022**, *13*, 1518. [CrossRef]
41. Mosre, J.; Suárez, F. Actual Evapotranspiration Estimates in Arid Cold Regions Using Machine Learning Algorithms with In Situ and Remote Sensing Data. *Water* **2021**, *13*, 870. [CrossRef]
42. Jahangir, M.H.; Arast, M. Remote sensing products for predicting actual evapotranspiration and water stress footprints under different land cover. *J. Clean. Prod.* **2020**, *266*, 121818. [CrossRef]
43. Wang, L.; Wang, J.J.; Ding, J.L.; Li, X. Estimation and Spatiotemporal Evolution Analysis of Actual Evapotranspiration in Turpan and Hami Cities Based on Multi-Source Data. *Remote Sens.* **2023**, *15*, 2565. [CrossRef]
44. Huayang, W.; Fengjiao, C.; Jun, L.; Kangjun, Q.; Gen, W. A study on spatial interpolation of temperature in Anhui Province based on ANUSPLIN. *Meteorol. Environ. Res.* **2019**, *10*, 51–60. [CrossRef]
45. McKenney, D.W.; Pedlar, J.H.; Papadopol, P.; Hutchinson, M.F. The development of 1901–2000 historical monthly climate models for Canada and the United States. *Agric. For. Meteorol.* **2006**, *138*, 69–81. [CrossRef]
46. Hameed, M.M.; AlOmar, M.K.; Razali, S.F.M.; Khalaf, M.A.K.; Baniya, W.J.; Sharafati, A.; AlSaadi, M.A. Application of Artificial Intelligence Models for Evapotranspiration Prediction along the Southern Coast of Turkey. *Complexity* **2021**, *2021*, 8850243. [CrossRef]

47. Cobaner, M.; Citakoglu, H.; Haktanir, T.; Kisi, O. Modifying Hargreaves-Samani equation with meteorological variables for estimation of reference evapotranspiration in Turkey. *Hydrol. Res.* **2017**, *48*, 480–497. [CrossRef]
48. Citakoglu, H.; Cobaner, M.; Haktanir, T.; Kisi, O. Estimation of Monthly Mean Reference Evapotranspiration in Turkey. *Water Resour. Manag.* **2014**, *28*, 99–113. [CrossRef]
49. Basakin, E.E.; Ekmekcioglu, Ö.; Özger, M.; Altinbas, N.; Saylan, L. Estimation of measured evapotranspiration using data-driven methods with limited meteorological variables. *Ital. J. Agrometeorol.-Riv. Ital. Di Agrometeorol.* **2021**, *1*, 63–80. [CrossRef]
50. Ma, L.; Zuo, C.Q. A comparison of spatial interpolation models for mapping rainfall erosivity on China mainland. *Advanced Mater. Res.* **2012**, *518–523*, 4489–4495. [CrossRef]
51. Paradise, T. *Turkey in Encyclopedia of World Geography*; Facts On File, Incorporated: New York, NY, USA, 2014.
52. Kuzucuoglu, C. *The Geomorphological Regions of Turkey: In Landscapes and Landforms of Turkey*; Springer International Publishing: Cham Switzerland, 2019.
53. Turkes, M. Climate and Drought in Turkey. In *Water Resources of Turkey*; Springer: Berlin/Heidelberg, Germany, 2020; pp. 85–125.
54. Bostan, P.; Heuvelink, G.B.; Akyurek, S. Comparison of regression and kriging techniques for mapping the average annual precipitation of Turkey. *Int. J. Appl. Earth Obs.* **2012**, *19*, 115–126. [CrossRef]
55. Deniz, A.; Toros, H.; Incecik, S. Spatial variations of climate indices in Turkey. *Int. J. Climatol.* **2011**, *31*, 394–403. [CrossRef]
56. Atalay, I. Vegetation. In *The Soils of Turkey*; Kapur, S., Akca, E., Gunal, H., Eds.; Springer International Publishing: Cham Switzerland, 2017.
57. Kazancı, N.; Kuzucuoğlu, C.L. *Threats and Conservation of Landscapes in Turkey: In Landscapes and Landforms of Turkey*; Springer: Cham Switzerland, 2019; pp. 603–632.
58. MGM. *Local Climate Parameters Between 1960–2017 for Turkey*; MGM: Ankara, Turkey, 2018.
59. Arikan, B.B.; Kahya, E. Homogeneity revisited: Analysis of updated precipitation series in Turkey. *Theor. Appl. Climatol.* **2019**, *135*, 211–220. [CrossRef]
60. Komuscu, A.U. Homogeneity analysis of long-term monthly precipitation data of Turkey. *Fresenius Environ. Bull.* **2010**, *19*, 1220–1230.
61. Türkeş, M.; Sümer, U.M.; Demir, İ. Re-evaluation of trends and changes in mean, maximum and minimum temperatures of Turkey for the period 1929–1999. *Int. J. Climatol. J. R. Meteorol. Soc.* **2002**, *22*, 947–977. [CrossRef]
62. Turkes, M.; Tatli, H. Use of the standardized precipitation index (SPI) and a modified SPI for shaping the drought probabilities over Turkey. *Int. J. Climatol.* **2009**, *29*, 2270–2282. [CrossRef]
63. NASA/METI/AIST. Japan Spacesystems and U.S./Japan ASTER Science Team. (2009). ASTER Global Digital Elevation Model [Data Set]. NASA EOSDIS Land Processes DAAC 2009. [CrossRef]
64. Bölük, E. *Climate in Turkey According to Thornthwaite Classification (In Turkish: Thornthwaite İklim Sınıflandırmasına Göre Türkiye İklimi)*; TC Orman Ve Su İşleri Bakanlığı Meteoroloji Genel Müdürlüğü, Araştırma Dairesi Başkanlığı: Ankara, Turkey, 2016; pp. 1–25.
65. Ozyuvaci, N. *Meteorology and Climatology*; Istanbul University, Faculty of Forestry: Istanbul, Turkey, 1999. (In Turkish)
66. Team, A.J.A.f.E. NASA EOSDIS Land Processes Distributed Active Archive Center (LP DAAC) at the USGS Earth Resources Observation and Science (EROS) Center. 2020. Available online: https://lpdaac.usgs.gov/resources/data-action/aster-ultimate-2018-winter-olympics-observer (accessed on 9 September 2022).
67. Tucker, C.J. Red and photographic infrared linear combinations for monitoring vegetation. *Remote Sens. Environ.* **1979**, *8*, 127–150. [CrossRef]
68. Dinerstein, E.; Olson, D.; Joshi, A.; Vynne, C.; Burgess, N.D.; Wikramanayake, E.; Hahn, N.; Palminteri, S.; Hedao, P.; Noss, R.; et al. An Ecoregion-Based Approach to Protecting Half the Terrestrial Realm. *BioScience* **2017**, *67*, 534–545. [CrossRef]
69. Hutchinson, M.F.; Xu, T. *Anusplin Version 4.4 User Guide*; Centre for Resource and Environmental Studies, The Australian National University: Canberra, Australia, 2004; p. 54.
70. Wahba, G. How to smooth curves and surfaces with splines and cross-validation. In Proceedings of the 24th Design of Experiments Conference, Madison, WI, USA, 23–25 October 1978; pp. 167–192.
71. Wahba, G. *Spline Models for Observational Data*; SIAM: New Delhi, India, 1990. [CrossRef]
72. Hutchinson, M. *The Application of Thin Plate Smoothing Splines to Continent-Wide Data Assimilation*; Bureau of Meteorology: Melbourne, Australia, 1991; pp. 104–113.
73. Zhang, X.; Shao, J.A.; Luo, H. Spatial interpolation of air temperature with Anusplin in Three Gorges Reservoir Area. In Proceedings of the 2011 International Conference on Remote Sensing, Environment and Transportation Engineering, Nanjing, China, 24–26 June 2011; pp. 3465–3468.
74. Craven, P.; Wahba, G. Smoothing noisy data with spline functions. *Numer. Math.* **1978**, *31*, 377–403. [CrossRef]
75. Chen, S.; Guo, J. Spatial interpolation techniques: Their applications in regionalizing climate-change series and associated accuracy evaluation in Northeast China. *J. Geomat. Nat. Hazards Risk* **2017**, *8*, 689–705. [CrossRef]
76. Mitas, L.; Mitasova, H. Spatial interpolation. In *Geographical Information Systems: Principles, Techniques, Management Applications*; Wiley: New York, NY, USA, 1999; p. 1.

77. Panigrahi, N. *Computing in Geographic Information Systems*; CRC Press: Boca Raton, FL, USA, 2014.
78. Beek, E. Spatial interpolation of daily meteorological data. *J. Theor. Eval. Available Techniques. Rep.* **1991**, *53*, 43.
79. Wu, Y.; Hung, M.-C. Comparison of spatial interpolation techniques using visualization and quantitative assessment. In *Applications of Spatial Statistics*; IntechOpen: London, UK, 2016; pp. 17–34. [CrossRef]
80. Ho, R. *Handbook of Univariate and Multivariate Data Analysis and Interpretation with SPSS*; CRC Press: Boca Raton, FL, USA, 2006.
81. International Business Machines Corporation (IBM). IBM SPSS Modeler Documentation Version 18.5. Available online: https://www.ibm.com/support/pages/spss-modeler-1821-documentation (accessed on 9 September 2024).
82. Prasad, R.K.; Bhimala, K.R.; Patra, G.K.; Himesh, S.; Goroshi, S. Annual and seasonal trends in actual evapotranspiration over different meteorological sub-divisions in India using satellite-based data. *Theor. Appl. Climatol.* **2023**, *152*, 999–1017. [CrossRef]
83. Yang, L.Y.; Shi, L.; Li, J.; Kong, H.; Wu, D.; Wei, J. Effects of climatic conditions and vegetation changes on actual evapotranspiration in Mu Us sandy land. *Water Sci. Technol.* **2023**, *88*, 723–737. [CrossRef]
84. Yao, T.C.; Lu, H.W.; Yu, Q.; Feng, S.S.; Xue, Y.X.; Feng, W. Uncertainties of three high-resolution actual evapotranspiration products across China: Comparisons and applications. *Atmos. Res.* **2023**, *286*, 106682. [CrossRef]
85. Jian, D.; Li, X.; Sun, H.; Tao, H.; Jiang, T.; Su, B.; Hartmann, H. Estimation of Actual Evapotranspiration by the Complementary Theory-Based Advection–Aridity Model in the Tarim River Basin, China. *J. Hydrometeorol.* **2018**, *19*, 289–303. [CrossRef]
86. Senay, G.B.; Friedrichs, M.; Morton, C.; Parrish, G.E.L.; Schauer, M.; Khand, K.; Kagone, S.; Boiko, O.; Huntington, J. Mapping actual evapotranspiration using Landsat for the conterminous United States: Google Earth Engine implementation and assessment of the SSEBop model. *Remote Sens. Environ.* **2022**, *275*, 113011. [CrossRef]
87. Yener, I. Development of high-resolution annual climate surfaces for Turkey using ANUSPLIN and comparison with other methods. *Atmosfera* **2023**, *37*, 425–444. [CrossRef]
88. Price, D.T.; McKenney, D.W.; Nalder, I.A.; Hutchinson, M.F.; Kesteven, J.L. A comparison of two statistical methods for spatial interpolation of Canadian monthly mean climate data. *Agric. For. Meteorol.* **2000**, *101*, 81–94. [CrossRef]
89. Zhao, H.; Huang, W.; Xie, T.; Wu, X.; Xie, Y.; Feng, S.; Chen, F. Optimization and evaluation of a monthly air temperature and precipitation gridded dataset with a 0.025° spatial resolution in China during 1951–2011. *Theor. Appl. Climatol.* **2019**, *138*, 491–507. [CrossRef]
90. Yuan, L.; Chen, X.; Ma, Y.; Han, C.; Wang, B.; Ma, W. A monthly 0.01° terrestrial evapotranspiration product (1982–2018) for the Tibetan Plateau. *Earth Syst. Sci. Data* **2022**, *2022*, 1–39.
91. Singh, R.; Senay, G.; Velpuri, N.; Bohms, S.; Verdin, J. On the Downscaling of Actual Evapotranspiration Maps Based on Combination of MODIS and Landsat-Based Actual Evapotranspiration Estimates. *Remote Sens.* **2014**, *6*, 10483–10509. [CrossRef]
92. Niu, Z.; He, H.; Zhu, G.; Ren, X.; Zhang, L.; Zhang, K.; Yu, G.; Ge, R.; Li, P.; Zeng, N.; et al. An increasing trend in the ratio of transpiration to total terrestrial evapotranspiration in China from 1982 to 2015 caused by greening and warming. *Agric. For. Meteorol.* **2019**, *279*, 107701. [CrossRef]
93. Rigden, A.J.; Salvucci, G.D. Evapotranspiration based on equilibrated relative humidity (ETRHEQ): Evaluation over the continental US. *Water Resour. Res.* **2015**, *51*, 2951–2973. [CrossRef]
94. Basconcillo, J.Q.; Duran, G.A.W.; Francisco, A.A.; Abastillas, R.G.; Hilario, F.D.; Juanillo, E.L.; Solis, A.L.S.; Lucero, A.J.R.; Maratas, S.L.A. Evaluation of Spatial Interpolation Techniques for Operational Climate Monitoring in the Philippines. *Sola* **2017**, *13*, 114–119. [CrossRef]
95. Maselli, F.; Angeli, L.; Battista, P.; Fibbi, L.; Gardin, L.; Magno, R.; Rapi, B.; Chiesi, M. Evaluation of Terra/Aqua MODIS and Sentinel-2 MSI NDVI data for predicting actual evapotranspiration in Mediterranean regions. *Int. J. Remote Sens.* **2020**, *41*, 5186–5205. [CrossRef]
96. Maselli, F.; Chiesi, M.; Angeli, L.; Fibbi, L.; Rapi, B.; Romani, M.; Sabatini, F.; Battista, P. An improved NDVI-based method to predict actual evapotranspiration of irrigated grasses and crops. *Agric. Water Manag.* **2020**, *233*, 106077. [CrossRef]
97. Adnan, R.M.; Heddam, S.; Yaseen, Z.M.; Shahid, S.; Kisi, O.; Li, B.Q. Prediction of Potential Evapotranspiration Using Temperature-Based Heuristic Approaches. *Sustainability* **2021**, *13*, 297. [CrossRef]
98. Sattari, M.T.; Apaydin, H.; Band, S.S.; Mosavi, A.; Prasad, R. Comparative analysis of kernel-based versus ANN and deep learning methods in monthly reference evapotranspiration estimation. *Hydrol. Earth Syst. Sci.* **2021**, *25*, 603–618. [CrossRef]
99. Cetin, M.; Alsenjar, O.; Aksu, H.; Golpinar, M.S.; Akgul, M.A. Comparing actual evapotranspiration estimations by METRIC to in-situ water balance measurements over an irrigated field in Turkey. *Hydrol. Sci. J.* **2023**, *68*, 1162–1183. [CrossRef]
100. Yang, Y.J.; Wang, S.J.; Bai, X.Y.; Tan, Q.; Li, Q.; Wu, L.H.; Tian, S.Q.; Hu, Z.Y.; Li, C.J.; Deng, Y.H. Factors Affecting Long-Term Trends in Global NDVI. *Forests* **2019**, *10*, 372. [CrossRef]
101. Pei, Z.F.; Fang, S.B.; Yang, W.N.; Wang, L.; Wu, M.Y.; Zhang, Q.F.; Han, W.; Khoi, D.N. The Relationship between NDVI and Climate Factors at Different Monthly Time Scales: A Case Study of Grasslands in Inner Mongolia, China (1982–2015). *Sustainability* **2019**, *11*, 7243. [CrossRef]
102. Zhang, H.X.; Chang, J.X.; Zhang, L.P.; Wang, Y.M.; Li, Y.Y.; Wang, X.Y. NDVI dynamic changes and their relationship with meteorological factors and soil moisture. *Environ. Earth Sci.* **2018**, *77*, 582. [CrossRef]

103. Gao, J.B.; Jiao, K.W.; Wu, S.H. Investigating the spatially heterogeneous relationships between climate factors and NDVI in China during 1982 to 2013. *J. Geogr. Sci.* **2019**, *29*, 1597–1609. [CrossRef]
104. Guo, L.; Wu, S.; Zhao, D.; Yin, Y.; Leng, G.; Zhang, Q. NDVI-Based Vegetation Change in Inner Mongolia from 1982 to 2006 and Its Relationship to Climate at the Biome Scale. *Adv. Meteorol.* **2014**, *2014*, 692068. [CrossRef]
105. Messaoud, Y.; Reid, A.; Tchebakova, N.M.; Goldman, J.A.; Hofgaard, A. The Historical Complexity of Tree Height Growth Dynamic Associated with Climate Change in Western North America. *Forests* **2022**, *13*, 738. [CrossRef]
106. Ergüner, Y.; Kumar, J.; Hoffman, F.M.; Dalfes, H.N.; Hargrove, W.W. Mapping ecoregions under climate change: A case study from the biological 'crossroads' of three continents, Turkey. *Landsc. Ecol.* **2019**, *34*, 35–50. [CrossRef]
107. Aktürk, E. Seasonal Vegetation Trends in Biomes of Türkiye: A Decade-Long (2014–2023) Analysis Using NDVI Time Series. *J. Bartin Fac. For.* **2024**, *26*, 230–243.
108. Zhan, Q.M.; Molenaar, M.; Tempfli, K.; Shi, W.Z. Quality assessment for geo-spatial objects derived from remotely sensed data. *Int. J. Remote Sens.* **2005**, *26*, 2953–2974. [CrossRef]
109. Visztra, G.V.; Frei, K.; Hábenczyus, A.A.; Soóky, A.; Bátori, Z.; Laborczi, A.; Csikós, N.; Szatmári, G.; Szilassi, P. Applicability of Point- and Polygon-Based Vegetation Monitoring Data to Identify Soil, Hydrological and Climatic Driving Forces of Biological Invasions-A Case Study of Ailanthus altissima, Elaeagnus angustifolia and Robinia pseudoacacia. *Plants* **2023**, *12*, 855. [CrossRef] [PubMed]
110. Del Grosso, S.J.; Parton, W.J.; Derner, J.D.; Chen, M.S.; Tucker, C.J. Simple models to predict grassland ecosystem C exchange and actual evapotranspiration using NDVI and environmental variables. *Agric. For. Meteorol.* **2018**, *249*, 1–10. [CrossRef]
111. Vatandaslar, C.; Türkes, M.; Semerci, A.; Karahan, A. Analyzing climate-induced mortality of Taurus fir based on temporal forest management plans and climatic variations and droughts in the Central Mediterranean sub-region of Turkey. *Eur. J. For. Res.* **2023**, *142*, 61–89. [CrossRef]
112. Albert, M.; Nagel, R.-V.; Sutmöller, J.; Schmidt, M. Quantifying the effect of persistent dryer climates on forest productivity and implications for forest planning. *For. Ecosyst.* **2018**, *5*, 7063. [CrossRef]
113. Yu, Y.; Zhou, Y.; Xiao, W.; Ruan, B.; Lu, F.; Hou, B.; Wang, Y.; Cui, H. Impacts of climate and vegetation on actual evapotranspiration in typical arid mountainous regions using a Budyko-based framework. *Hydrol. Res.* **2020**, *52*, 212–228. [CrossRef]
114. Abbasi, N.; Nouri, H.; Didan, K.; Barreto-Muñoz, A.; Chavoshi Borujeni, S.; Salemi, H.; Opp, C.; Siebert, S.; Nagler, P. Estimating Actual Evapotranspiration over Croplands Using Vegetation Index Methods and Dynamic Harvested Area. *Remote Sens.* **2021**, *13*, 5167. [CrossRef]
115. Nouri, H.; Beecham, S.; Anderson, S.; Nagler, P. High Spatial Resolution WorldView-2 Imagery for Mapping NDVI and Its Relationship to Temporal Urban Landscape Evapotranspiration Factors. *Remote Sens.* **2014**, *6*, 580–602. [CrossRef]
116. Zhao, T.X.; Zhu, Y.; Ye, M.; Yang, J.Z.; Jia, B.A.; Mao, W.; Wu, J.W. A new approach for estimating spatial-temporal phreatic evapotranspiration at a regional scale using NDVI and water table depth measurements. *Agric. Water Manag.* **2022**, *264*. [CrossRef]
117. Pieri, M.; Cantini, C.; Giovannelli, A.; Maselli, F.; Chiesi, M.; Battista, P.; Fibbi, L.; Gardin, L.; Rapi, B.; Romani, M.; et al. Estimation of Actual Evapotranspiration in Fragmented Mediterranean Areas by the Spatio-Temporal Fusion of NDVI Data. *IEEE J. Sel. Top. Appl. Earth Obs. Remote Sens.* **2019**, *12*, 5108–5117. [CrossRef]
118. Joiner, J.; Yoshida, Y.; Anderson, M.; Holmes, T.; Hain, C.; Reichle, R.; Koster, R.; Middleton, E.; Zeng, F.W. Global relationships among traditional reflectance vegetation indices (NDVI and NDII), evapotranspiration (ET), and soil moisture variability on weekly timescales. *Remote Sens. Environ.* **2018**, *219*, 339–352. [CrossRef] [PubMed]
119. Mo, X.; Liu, S.; Lin, Z.; Wang, S.; Hu, S. Trends in land surface evapotranspiration across China with remotely sensed NDVI and climatological data for 1981–2010. *Hydrol. Sci. J.* **2015**, *60*, 2163–2177. [CrossRef]
120. Giarolla, A.; Baethgen, W.E.; Ceccato, P. *NDVI (Modis Sensor) Response to Interannual Variability of Rainfall and Evapotranspiration in a Soybean Producing Region*. Southern Brazil. 2010, pp. 219–224. Available online: https://www.isprs.org/proceedings/XXXVIII/part7/b/pdf/219_XXXVIII-part7B.pdf (accessed on 2 January 2023).
121. Galvíncio, J.D.; Silva, H.A.d.; Popescu, S.S. Analysis of influence of evapotranspiration on rainfall in an Atlantic forest using remote sensing data. *Rev. Bras. De Geogr. Física* **2014**, *7*, 17–33. [CrossRef]
122. Jaramillo, F.; Cory, N.; Arheimer, B.; Laudon, H.; van der Velde, Y.; Hasper, T.B.; Teutschbein, C.; Uddling, J. *The Effect of Northern Forest Expansion on Evapotranspiration Overrides that of a Possible Physiological Water Saving Response to Rising CO_2: Interpretations of Movement in Budyko Space*. 2017, p. 24. Available online: https://hess.copernicus.org/preprints/hess-2017-347/hess-2017-347.pdf (accessed on 9 September 2024).
123. Cernohous, V.; Sach, F.; Kantor, P.; Svihla, V.J.E.R.; InTech. *Methods of Evapotranspiration Assessment and Outcomes From forest Stands and a Small Watershed*; IntechOpen: London, UK, 2011; pp. 73–102.